SLAC-PUB-14355

Three years *Swift*–BAT Survey of AGN: reconciling theory and observations?*

D. Burlon[1],

burlon@mpe.mpg.de

M. Ajello[2],

majello@slac.stanford.edu

J. Greiner[1], A. Comastri[3], A. Merloni[1,4], and N. Gehrels[5]

ABSTRACT

It is well accepted that unabsorbed as well as absorbed AGN are needed to explain the nature and the shape of the Cosmic X-ray background, even if the fraction of highly absorbed objects (dubbed Compton-thick sources) substantially still escapes detection. We derive and analyze the absorption distribution using a complete sample of AGN detected by *Swift*–BAT in the first three years of the survey. The fraction of Compton-thick AGN represents only 4.6% of the total AGN population detected by *Swift*–BAT. However, we show that once corrected for the bias against the detection of very absorbed sources the real intrinsic fraction of Compton-thick AGN is 20^{+9}_{-6} %. We proved for the first time (also in the BAT band) that the anti-correlation of the fraction of absorbed AGN and luminosity it tightly connected to the different behavior of the luminosity functions (XLFs) of absorbed and unabsorbed AGN. This points towards a difference between the two subsamples of objects with absorbed AGN being, on average,

[1]Max-Planck-Institut für Extraterrestrische Physik, Giessenbachstraße 1, 85740 Garching, Germany

[2]SLAC National Laboratory and Kavli Institute for Particle Astrophysics and Cosmology, 2575 Sand Hill Road, Menlo Park, CA 94025, USA

[3]INAF Osservatorio Astronomico di Bologna, via Ranzani 1, 40127 Bologna, Italy

[4]Excellence Cluster Universe, TUM, Boltzmannstraße 2, 85748, Garching, Germany

[5]Astrophysics Science Division, Mail Code 661, NASA Goddard Space Flight Center, Greenbelt, MD 20771, USA

*Based on observations obtained with XMM-Newton, an ESA science mission with instruments and contributions directly funded by ESA Member States and NASA.

Work supported in part by US Department of Energy contract DE-AC02-76SF00515.

SLAC National Accelerator Laboratory, Menlo Park, CA 94025

intrinsically less luminous than unobscured ones. Moreover the XLFs show that the fraction of obscured AGN might also decrease at very low luminosity. This can be successfully interpreted in the framework of a disk cloud outflow scenario as the disappearance of the obscuring region below a critical luminosity. Our results are discussed in the framework of population synthesis models and the origin of the Cosmic X-ray Background.

Subject headings: X-rays: general – Radiation mechanisms: non-thermal – X-rays: observations – Galaxies: active

1. Introduction

It is well known that absorbed active galactic nuclei (AGN) are needed to explain the shape of the Cosmic X-ray background (CXB) spectrum (e.g. Gilli et al. 2007; Treister et al. 2009). A large fraction of them is indeed detected in the shallow and deep $< 10\,\mathrm{keV}$ X-ray surveys (see e.g. Brandt & Hasinger 2005). Nonetheless, a large fraction of Compton-thick ($\mathrm{N}_H \geq 1.5 \times 10^{24}\,\mathrm{H\text{-}atoms\ cm^{-2}}$, for a review see Comastri 2004) AGN still escapes detection. Because of their large absorbing column density, these sources contribute a ∼10–25% fraction of the CXB emission (Gilli et al. 2007; Treister et al. 2009, respectively) at 30 keV, but at the same time are expected to be fairly numerous representing up to $\sim 30\,\%$ of the entire AGN population (Risaliti et al. 1999; Worsley et al. 2005) . The advent of sensitive all-sky surveys above 15 keV (e.g. *Swift*–BAT and INTEGRAL) opened the possibility to detect these objects. Indeed, it is above 10–15 keV that part of the primary continuum emission pierces through the veil of Compton-thick material, making it easier for these objects to be detected. Despite this fact, the early results from the *Swift* and INTEGRAL surveys showed that the fraction of Compton-thick AGN is merely a 5–10% of the total AGN population (see Ajello 2009, and references therein). Thus it might be that the fraction of Compton-thick AGN is intrinsically smaller than previously determined. Nevertheless, it should be taken into account that even above $> 15\,\mathrm{keV}$, instruments are biased against the detection of $\log \mathrm{N}_H > 24$ sources. Indeed as shown in e.g. Ghisellini et al. (1994), Ajello (2009), 50% of the source flux (between 15-55 keV) is lost if $\log \mathrm{N}_H > 24.5$. The fact that three of the closest AGN ever detected (i.e. NGC 1068, Circinus galaxy and NGC 4945) are absorbed by $\mathrm{N}_H \geq 10^{24}\,\mathrm{atoms\ cm^{-2}}$ suggests that indeed this is the likely explanation.

In this work, we present and discuss the results of the most complete - until now - survey of AGN in the local Universe (z<0.1) using data from the *Swift*–BAT telescope. We performed a detailed spectral study of the three years sample of Seyfert-like objects by combining the hard X-ray information with the soft X-ray observations realized by different

missions in the recent past. To this aim we extracted *Swift*–BAT spectra and spectra in the 0.3–10 keV band using archival *XMM–Newton* and *Swift*–XRT data. In a handful of cases we requested and obtained target-of-opportunity (ToO) observations with *Swift* for objects without previous coverage at soft X-rays. The use of X-ray data in the 0.3–195 keV band allows us to constrain robustly all the source parameters (including the absorbing column density).

This paper is organized as follows. In §2 we present the sample and discuss how the joint spectral analysis was performed. The general properties of the 15–195 keV continuum of AGN, the stacked analysis for the absorbed, unabsorbed, and Compton-thick spectra are presented in §3. §4 presents the observed N_H distribution. We then evaluate, for the BAT survey, the bias against the detection of the most obscured AGN and estimate -for the first time- the intrinsic absorption distribution. §5 presents the anti-correlation between the fraction of absorbed AGN (relative to the whole population) and luminosity, while the luminosity functions of AGN are derived in §6. The results of these analyses are discussed in §7 while §8 summarizes our findings. In this work we use a standard cosmology ($H_0 = 70$, $q_0 = 0$, and $\Omega_\Lambda = 0.73$).

2. The *Swift*–BAT sample and data analysis

2.1. The sample

The Burst Alert Telescope (BAT; Barthelmy et al. 2005) onboard the *Swift* satellite (Gehrels et al. 2004), represents a major improvement in sensitivity for imaging of the hard X-ray sky. BAT is a coded mask telescope with a wide field of view (FOV, $120^\circ \times 90^\circ$ partially coded) aperture, sensitive in the 15–200 keV domain. Thanks to its wide FOV and its pointing strategy, BAT monitors continuously up to 80% of the sky every day achieving, after several years of the survey, deep exposure in the entire sky. Results of the BAT survey (Markwardt et al. 2005; Ajello et al. 2008a; Tueller et al. 2010) show that BAT reaches a sensitivity of $\sim$1 mCrab[1] in 1 Ms of exposure. Being the BAT survey not a flux-limited survey, but rather a significance-limited one, it is important to address how the survey flux limit changes over the sky area. This is often referred to as sky coverage, that is the distribution of the surveyed area as a function of limiting flux. Its knowledge is very important when performing population studies as the ones described in the next sections. The reader is referred to Ajello et al. (2008a) for how to derive the sky coverage as a function

[1] 1 mCrab in the 15–55 keV band corresponds to 1.27×10^{-11} erg cm^{-2} s^{-1}

of the minimum detectable flux F_{min}. This is defined as the sum of the area covered to fluxes $f_i < F_{min}$:

$$\Omega(< F_{min}) = \sum_{i}^{N} A_i \ , f_i < F_{min} \quad (1)$$

where N is the number of image pixels and A_i is the area associated to each of them. A visual representation of the sky coverage is reported in Ajello et al. (2009b) which shows clearly the good sensitivity of BAT. The survey, in our analysis (15–55 keV), reaches a limiting sensitivity of ∼0.6 mCrab (7.3×10^{-12} erg cm^{-2} s^{-1}). We *ex post* checked that cutting the sample at 50 % of the complete sky coverage (i.e. at 1.1×10^{-11} erg cm^{-2} s^{-1}) does not affect significantly the findings of this work, since the 35 objects below this limit do not populate a particular N_H range.

The sample used in this work is the collection of non-blazar AGN detected by BAT during the first three years, more precisely between March 2005 and March 2008. This sample is part of the one used in Ajello et al. (2009b) which comprises all sources detected by BAT at high (|b|>15°) Galactic latitude and with a signal-to-noise ratio (S/N) exceeding $5\,\sigma$. All the 199 sources which are identified as non-blazar AGN (e.g. Seyferts) constitute the sample used in this work and are reported (along with their properties) in the table at the end of the paper. Note that the main sample, from which the sub-sample of AGN is derived, comprises 307 objects of which only 7 are as of today without identification. The incompleteness or the parent population is thus 2.3 %. We note that in our sample 19 objects are classified as 'Galaxies' or 'Liners'. We believe these are normal AGN (e.g. Seyfert galaxies) for which an accurate optical classification is not yet available in the literature. This is based on the fact that the average redshift, luminosity and absorbing column density are respectively 0.03, $4.5{\times}10^{43}$erg s^{-1} and 10^{23} cm^{-2}. These values are in good agreement with the ones derived from the rest of the sample giving confidence to our hypothesis that these objects are AGN.

2.2. Extraction of *Swift*–BAT spectra

For each source in our sample we extracted a 15–195 keV spectrum following the method described in Ajello et al. (2008c). Here we recall the main steps: the details can be found in the aforementioned paper. For a given source, we extract a 12 channel spectrum from each observation where the source is in the field of view. These spectra are corrected for residual background contamination and for vignetting; the per-pointing spectra are then (weighted) averaged to produce the final source spectrum. Thus, the final spectrum represents the average source emission over the time-span considered here (three years). Moreover the

reader is referred to Ajello et al. (2009a) for a discussion about the accuracy of the spectra extracted with this method.

2.3. Extraction of the soft X-ray spectra

The goal of the present work is to obtain a reliable estimate of the intrinsic absorbing column density for the BAT AGN. 102 objects (out of the 199 AGN in our sample) have a reliable estimate of the absorbing column density present in the literature. The large majority (86) of these N_H measurements comes from earlier results of the *Swift* survey (Tueller et al. 2008; Winter et al. 2008, 2009a,b) while for the rest (16) we used single-source publications (see the table at the end of the paper for details).

For all the objects without a N_H measurement we used the available follow-up observations performed by two observatories (i.e. *Swift*–XRT and *XMM–Newton* in 83 and 12 cases, respectively). XRT was used preferentially, while *XMM–Newton* was used in a handful of cases (i.e. when the detection significance by *Swift*–XRT was too low to constrain the spectral parameters and/or the N_H). Only in 2 cases we could not find any XRT or XMM follow up (i.e. 1H 2107-097) or the available soft X-ray pointing was not deep enough to extract a spectrum of the source (i.e. [VV2003c] J014214.0+011615).

For the filtering and spectra extraction we used `xrtproducts` only on Photon Counting Level 2 event files (grades 0–12) and the standard ftools of *Headas v6.6.3* software, and *SAS v9.0.0* for *Swift*–XRT and *XMM–Newton* observations respectively. We used *Xspec* v12.4.0*ad* (Arnaud 1996) to perform, for each AGN, joint spectral fits between the 15–195 keV and the 0.3–10 keV data. Normally the spectra of sources detected (in the 0.3–10 keV band) with sufficient S/N were re-binned as to have a minimum of 20 counts/bin. In a handful of cases spectra were re-binned as to have 10 counts/bin, and consequently Cash in place of χ^2 statistics was adopted.

During the spectral fitting stage we took into account, regardless of the spectral model used (i) the local Galactic absorption (Kalberla et al. 2005) and (ii) a normalization factor to account for the different inter-calibration of the two instruments and for a possible variation of the source between the observation epochs. Small differences in the computed value of N_H might be present when comparing observations taken at different times. The case of NGC 7582 is discussed in §4.2, but in general we warn that variations of the column densities are expected (see e.g. Risaliti et al. 2002, 2009; Bianchi et al. 2009a, and references therein).

3. General properties

We discuss in the following the general properties of the sample, focussing on the hard X-ray continuum emission. The joint analysis is considered in this section only to the aim of splitting the parent population in un-absorbed and absorbed sources. Fig. 1 shows the luminosity-redshift plane for all the AGN in the BAT sample. The $k-$corrected L_X luminosities (not corrected for absorption, but see §3.2 and §4.2) were computed according to:

$$L_X \; = \; 4\pi d_{\rm L}^2 \frac{F_X}{(1+z)^{2-\Gamma_X}} \tag{2}$$

where F_X is the X-ray flux in the 15–55 keV energy range as listed in the table at the end of the paper (see Ajello et al. 2008b, for details about the flux determination), and Γ_X is the photon spectral index. Throughout this work, absorbed sources are those with an absorbing column density ($N_{\rm H}$) larger than (or equal to) 10^{22} atoms cm^{-2}. It is apparent from Fig. 1 that obscured AGN populate more densely the low-luminosity/low-redshift part of the graph with respect to the high-luminosity/high-redshift part. A Kolmogorov-Smirnov (KS) test between the redshifts of the two populations of AGN (absorbed and unabsorbed) shows that the probability that both classes are drawn from the same parent population is $\sim 1.4 \times 10^{-3}$.

The lines reported in Fig. 1 represent the current limiting flux of the BAT survey ($\sim 7.3 \times 10^{-12}$ erg cm^{-2} s^{-1}, solid line) and a much brighter flux of 10^{-10} erg cm^{-2} s^{-1} (dashed line). In the shallower case it is apparent that sources detected are preferentially absorbed with log$N_{\rm H}$ larger than 22.

3.1. Analysis of the 15-195 keV continuum

We performed a simple power-law fit to the BAT spectra in the 15–195 keV band to derive a measurement of the photon index. These values are reported in the last table with the corresponding 90% uncertainties. The distribution of photon indices of all the BAT AGN is compatible with a Gaussian distribution with a mean of 1.95±0.02 and a sigma of 0.27±0.02. We analyzed separately the distribution of photon indices of obscured and unobscured sources respectively. These are reported in Fig. 2. We find that the two distributions appear to be different with the one of obscured sources showing a mean of 1.92±0.02 and a sigma of 0.25±0.02 while the one of unobscured AGN displays a mean of 2.07±0.03 and a sigma of 0.27±0.03. This is also confirmed by the Kolmogorov-Smirnov test which yields a probability of 3×10^{-3} that the two distributions are drawn from the same parent population. The CT sources are not the main drivers of the distribution of

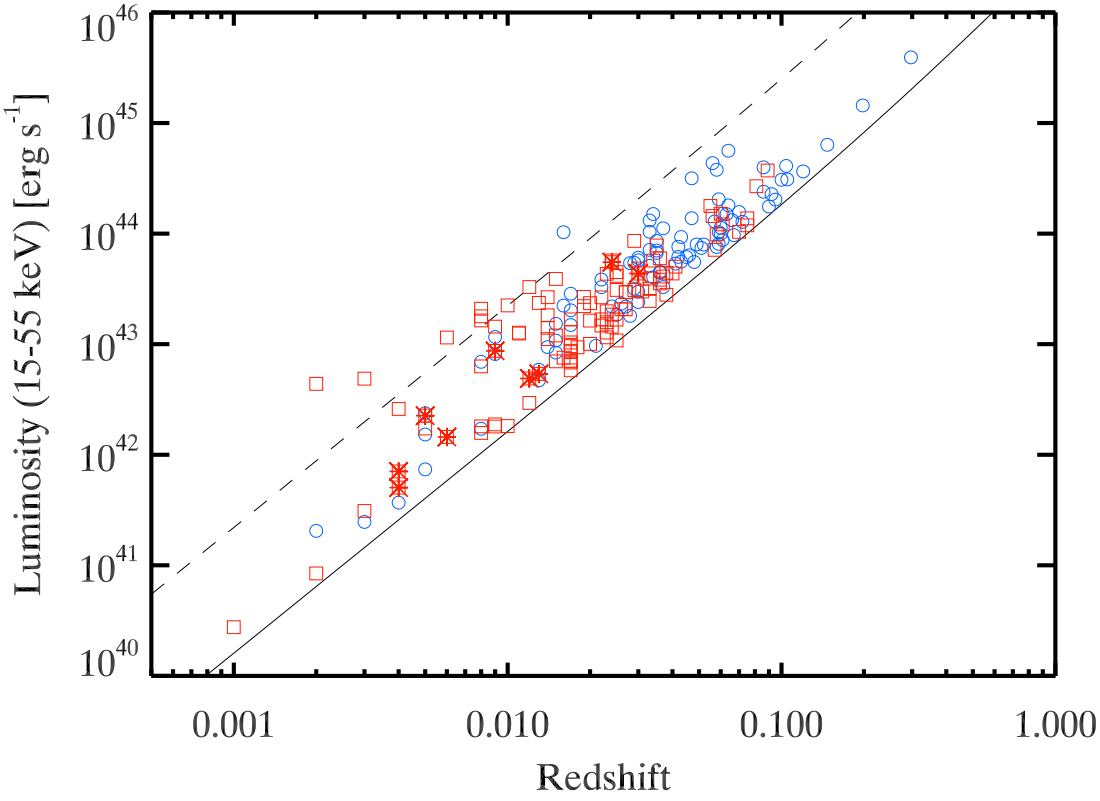

Fig. 1.— Luminosity-redshift plane for unabsorbed sources (blue circles) and for absorbed sources (red squares). The solid line represents the limiting sensitivity of the *Swift*–BAT survey for a source with photon index equal to 1.9, while the dashed line represents the sensitivity of the survey at a brighter flux, i.e. 10^{-10} erg cm^{-2} s^{-1}.

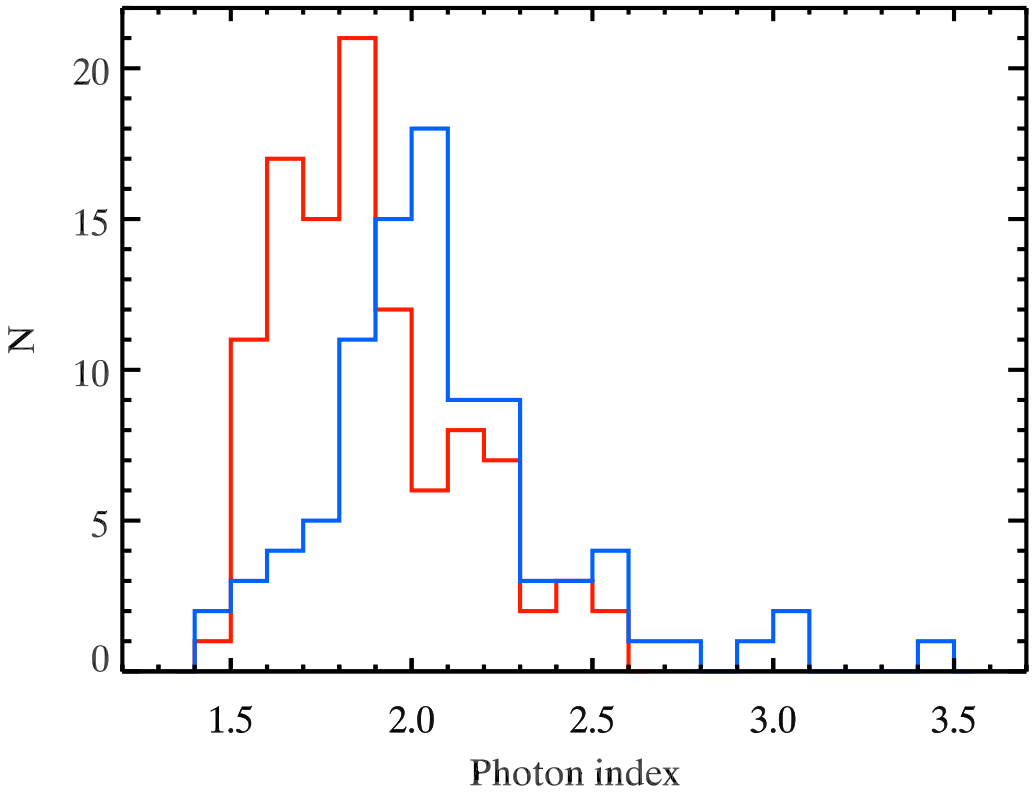

Fig. 2.— Photon indices distribution of absorbed AGN ($\log N_H \geq 22$, red line) and unabsorbed AGN ($\log N_H < 22$, blue line). The photon indices used are the ones derived in the BAT band only (i.e. 15–195 keV band) and reported in the table at the end of the paper.

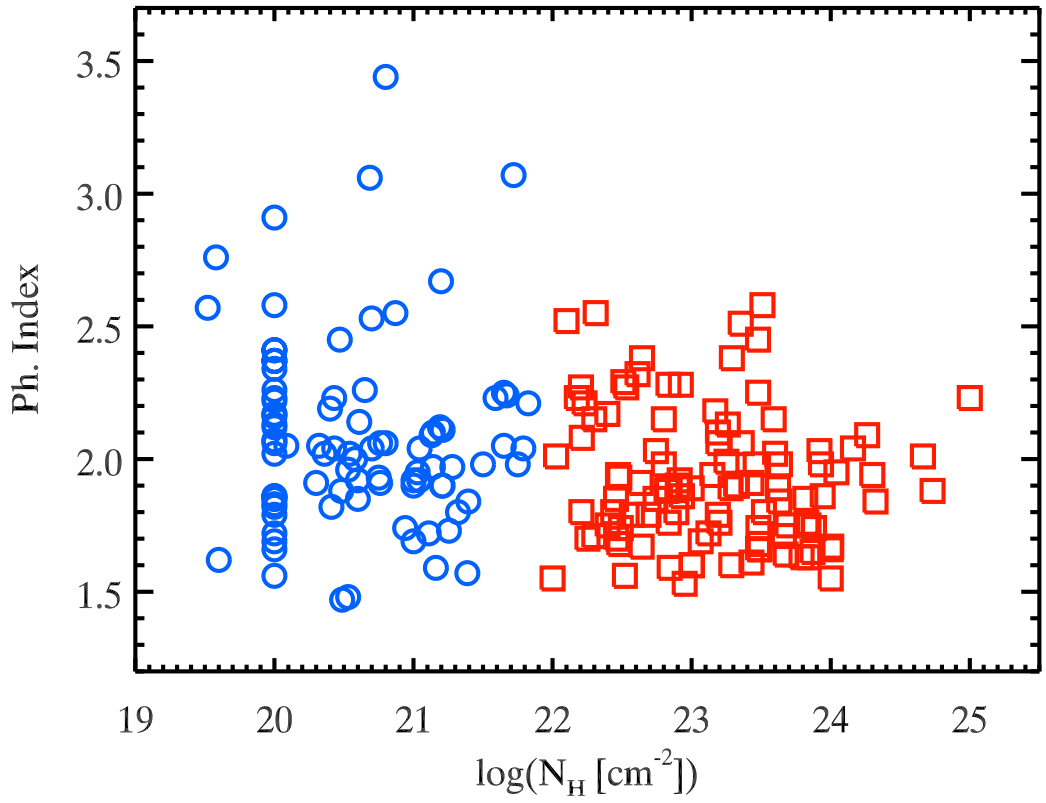

Fig. 3.— Photon spectral index as obtained from fitting with a simple power-law the BAT spectrum alone, versus the N_H found from the combined spectra in the 0.3–195 keV energy range. Different color/symbol identify absorbed and unabsorbed sources.

absorbed sources. Indeed eliminating the 9 most absorbed sources from the sample does not in turn introduce an appreciable difference in the distribution. The KS test returns a null probability of $\sim 1 \times 10^{-3}$ in this case. Thus, there is an indication, albeit marginal, that absorbed sources display, on average, a harder power-law continuum than unobscured ones.

According to Hopkins et al. (2009) radiatively inefficient accretion flows (RIAFs) make the intrinsic X-ray spectrum of an AGN harder. This may cause to incorrectly classify, at energies below <10 keV, an AGN as obscured if only simple estimators (e.g. hardness ratios) are used. This is not however the case for the present work, because: 1) BAT is able to sample the intrinsic power-law spectral index independently of the level of absorption, 2) all sources have sufficient signal-to-noise ratio to correctly derive the absorption level using *XMM–Newton* or *Swift*–XRT data in conjunction with BAT ones. Thus, while RIAFs might certainly affect the intrinsic shape of the 15-195 keV continua, we believe that the differences observed here are ascribed to orientation effects (as shown already in Ajello et al. 2008c). As it can be seen in Fig. 3 we show the scatter plot of photon indices versus the absorbing column density and indeed there is a weak indication of a correlation between the two parameters (the Spearman's rank is -0.27, and null hypothesis probability $P \sim 1.2 \times 10^{-4}$). The low, negative rank correlation coefficient and the P value indicate that a chance correlation can be excluded at more than the $\gtrsim 3\sigma$ level. However if the sources with unconstrained N_H are excluded from the sample the correlation is not statistically significant any longer ($P = 1.3 \times 10^{-3}$). A mild correlation is anyway expected, because of the contribution of the higher reflection component of type 1 AGN, in the low energy channel of the BAT. The "softening" effect that is introduced when fitting with a simple power-law is further discussed in the following section.

We note that three AGN (i.e. Mrk 766, IRAS 05480+5927, Mrk 739) show a very soft BAT spectrum (e.g. photon index >3). For Mrk 766 we analyzed XRT and BAT data jointly and found out that the intrinsic power-law seems to be ∼2.0 and that indeed a large reflection component is required (the data show also the presence of a soft excess). The large reflection component is what makes (very likely) the BAT spectrum softer. The BAT spectrum of IRAS 05480+5927 is quite noisy and very soft. Nonetheless by a joint fit with XRT the photon index is constrained to be ∼1.8. A cutoff-powerlaw is statistically (ftest probability $> 3\sigma$) better but in turn requires the cutoff energy to be at 18 keV (in the 12–30 keV range, 3σ contours). As for Mrk 739, a joint fit with XRT gives a slope of 1.7. We note that again a cutoff-powerlaw is statistically preferred with a cutoff energy of ~ 50 keV. Our results are unaffected by the change of these three BAT-soft spectra to the flatter value reported for the joint analysis.

Stacked spectra analysis – In order to investigate the global spectral properties of AGN

Table 1: Best-fit parameters for the stacked spectra. Errors are 90 % CL and parameters without an error were kept fixed during the fitting stage. The columns report the value of the photon index (Γ), normalization of the reflection component R, the cut-off energy E_c and the absorption.

SAMPLE	# Obj	Γ	R	E_c (keV)	$N_{\rm H}$ (10^{22} cm^{-2})	χ^2/dof
All	199	$1.78^{+0.25}_{-0.39}$	< 4.50	> 80	–	5.2/8
All	199	$1.80^{+0.08}_{-0.08}$	$1.00^{+0.48}_{-0.36}$	300	–	5.2/9
Absorbed[1]	96	$1.74^{+0.07}_{-0.07}$	$0.55^{+0.67}_{-0.35}$	300	–	3.3/9
Unabsorbed[1]	92	$1.71^{+0.10}_{-0.06}$	$1.23^{+1.12}_{-1.00}$	300	–	3.6/9
Compton-thick	9	1.80	–	88^{+35}_{-21}	265^{+171}_{-131}	9.6/9

[1] For absorbed and unabsorbed AGN we have assumed that the inclination angle between the normal to the disk/torus and the line of sight is 60 and 30 degrees respectively. The class of absorbed AGN includes all AGN which are absorbed but are not Compton-thick (e.g. 22≤LogN$_{\rm H}$ ≤24). We did not include the 2 AGN for which N$_{\rm H}$ could not be calculated.

we performed a stacking analysis of the AGN in the BAT sample. The stacked spectrum of several sources is produced performing the weighted average of all the spectra. The weight is chosen to be the inverse of the variance of a given bin and it is exactly the same procedure used to extract the spectra of each individual source. The same stacking technique has been already applied with success to both the study of Seyfert galaxies and galaxy clusters detected by BAT (Ajello et al. 2008b, 2009a). This stacking technique is appropriate for the stacking of background-subtracted spectra generated by coded masks telescopes. As already reported in Ajello et al. (2009a), this stacking technique allows to determine the average properties of a source population. The stacked spectrum of the 199 AGN is not compatible with a simple power law (χ^2/dof = 22.62/10). This is due to a substantial curvature of the spectrum around 30 keV (see Fig. 4). We found that an acceptable fit to the data ($\chi^2/dof = 5.2/8$) is achieved when using a PEXRAV model. In this case we find that the best fit parameter for the slope is $1.78^{+0.25}_{-0.39}$ (error are 90 % CL). Given the small dynamic range of the BAT spectrum (15–195 keV) is impossible to disentangle uniquely the reflection component and the cut-off energy. Indeed, our best fit shows that, at 90 % confidence, the normalization of the reflection component is consistent with zero while the cut-off energy is bound to be $\geq$ 80 keV. The parameters of this best fit are reported in Tab. 1. In order to avoid this degeneracy we fixed the cut-off energy at 300 keV (see Dadina 2008, which reported an average cut-off of 300 keV for *BeppoSAX* sources). The best fit parameters (reported also in Tab. 1) for the photon index and the reflection are respectively $1.80^{+0.08}_{-0.08}$ and $1.00^{+0.48}_{-0.36}$, which are in good agreement with the findings of Nandra & Pounds (1994). The normalization of the reflection component is compatible with the presence of a reflecting medium which covers an angle of 2π at the nuclear source.

In addition we generated stacked spectra for unabsorbed (logN$_{\rm H}$ $<$ 22), absorbed

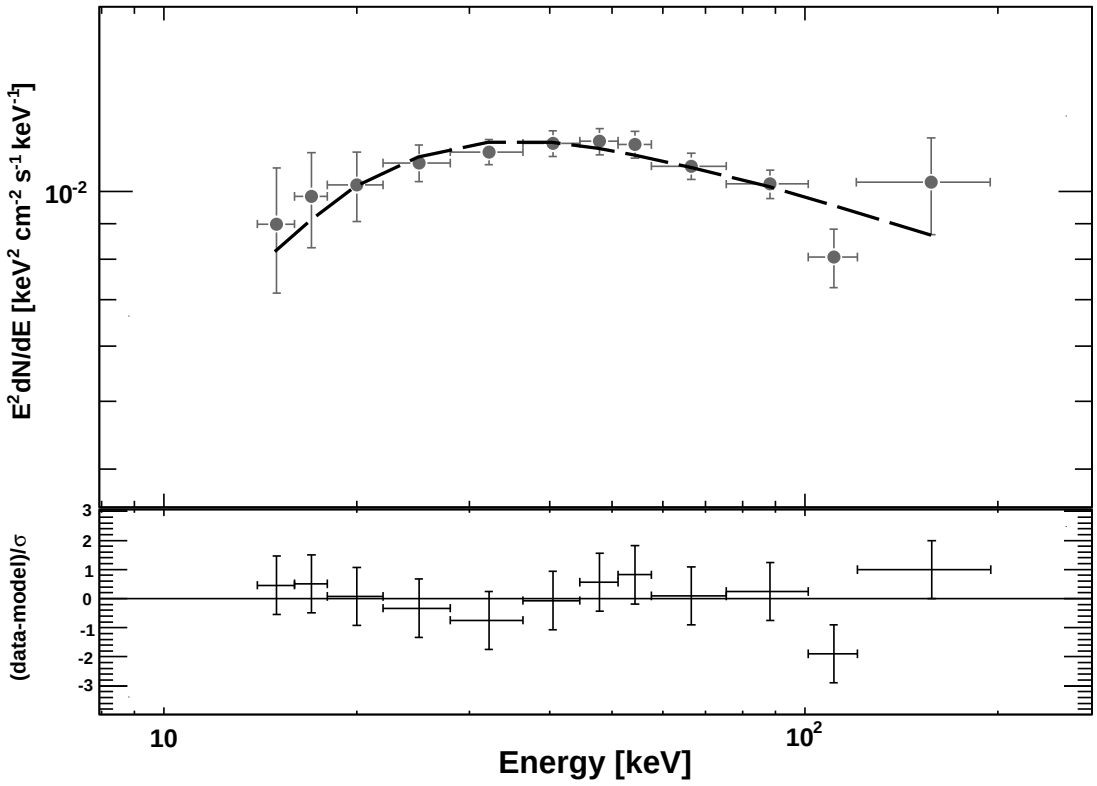

Fig. 4.— Stacked spectrum of the 199 Swift AGN. The dashed line is the best-fit PEXRAV model. Note the substantial curvature of the spectrum around ∼30–40 keV.

($22 \leq \log N_H \leq 24$) and Compton-thick ($\log N_H > 24$) AGN. A simple power-law fit to the spectra of unabsorbed and absorbed AGN yields that the best-fit photon indices are 2.13±0.06 and 2.00±0.06 respectively. This is found to be in agreement with what derived from the analysis of the photon index of the two distributions: i.e. on average unabsorbed AGN have steeper spectra than absorbed ones. The indices derived from the stacking analysis are slightly steeper than the average ones derived from the photon index distribution because the stacked spectra show a significant curvature which makes the simple power-law fit not the most accurate one (e.g. reduced $\chi^2 \geq 2.0$). We thus decided to fit the stacked spectra with a PEXRAV model. Also in the stacked spectra of absorbed and unabsorbed AGN the cut-off energy and the reflection component cannot be determined uniquely. We thus fixed the cut-off energy to 300 keV. A fit to the stacked spectrum of absorbed sources yields a photon index of $1.74^{+0.07}_{-0.07}$, and a reflection component of $R=0.55^{+0.67}_{-0.35}$.

The fit to the stacked spectrum of unobscured sources yields a photon index of $1.71^{+0.10}_{-0.06}$ and a reflection component of $R=1.23^{+1.12}_{-1.00}$. The uncertainties are large, however these results (which are reported in Tab. 1) seem consistent with the unified model which predicts a larger reflection component for unobscured sources (for a discussion see e.g. Ajello et al. 2008a, and references therein). In addition, our findings agree with the modeling of obscured sources in Gilli et al. (2007), where the reflection efficiency for high inclination angles (expected for obscured AGN in the unified picture) is lower (0.88 rather than 1.3) than the one assumed for unobscured ones.

3.1.1. The 15–195 keV Spectrum of Compton-thick AGN

Finally we also investigate, for the first time, the average spectrum of Compton-thick AGN. Our first goal is to determine an empirical model which describes the 15-200 keV emission of Compton-thick AGN reasonably well and then later to interpret the features of the spectrum. Thus, we started fitting the stacked spectrum of the 9 Compton-thick AGN with a simple power-law model. The best-fit photon index is 2.04±0.09, but because of the spectral curvature this model represents a poor description of the data (χ^2/dof=42.1/10). The fit improves (χ^2/dof=16.1/9) if we use an absorbed power-law model. In this case the best-fit photon index and absorbing column density are respectively $2.48^{+0.21}_{-0.18}$ and $N_H = 4.7^{+2.4}_{-1.9} \times 10^{24}\,\mathrm{cm}^{-2}$. As a last step we tried to fit the stacked spectrum with an absorbed cut-off power-law model. We fixed the photon index of the power law to 1.8 to avoid degeneracy among the parameters. This model provides a good representation of the BAT data (χ^2/dof=9.7/9). The column density is consistent with being Compton-thick ($N_H = 289^{+163}_{-131} \times 10^{22}\,\mathrm{atoms\ cm}^{-2}$) and the cut-off energy is 82^{+39}_{-19} keV. The results of this fit are

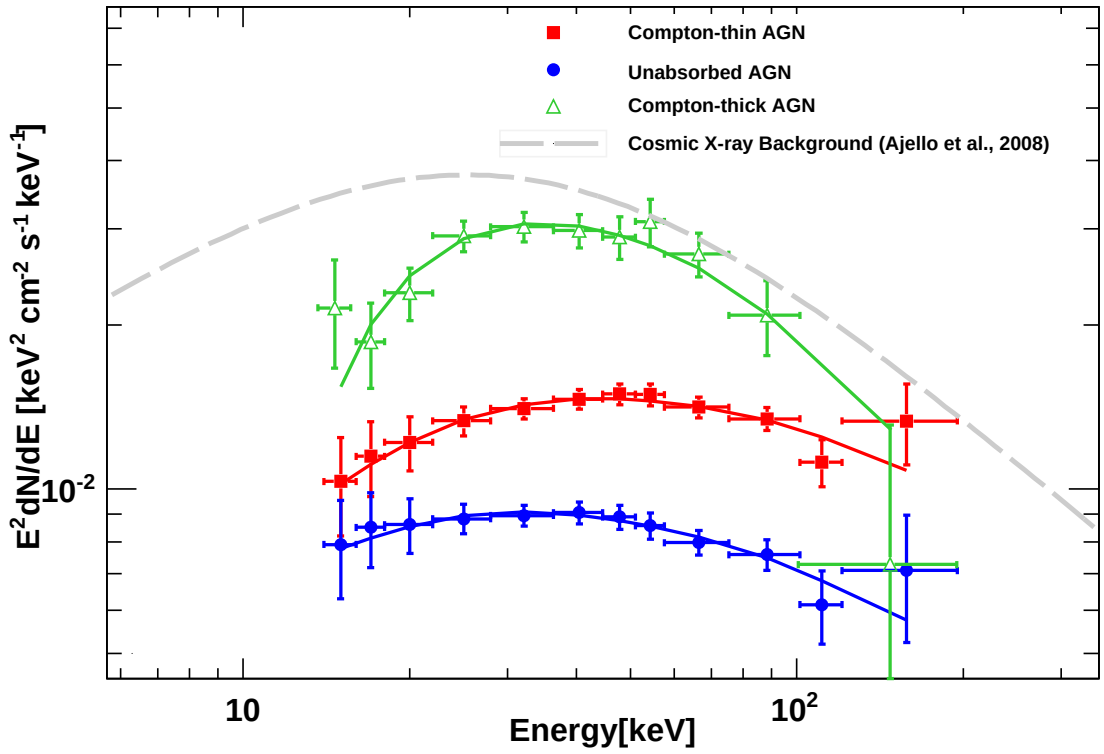

Fig. 5.— Stacked spectra of obscured AGN (22 $\leq$logN$_{\rm H}$ $\leq$ 24), unabsorbed AGN (logN$_H$ $<$ 22) and Compton-thick AGN (logN$_{\rm H}$ $>$ 24) compared to the Cosmic X-ray background (CXB) as measured by Ajello et al. (2008b). Note that both the CXB spectrum and the spectrum of Compton-thick AGN have been rescaled arbitrarily.

summarized in Tab. 1. However, we caution the reader this model (zphabs in *Xspec*) takes into account only photoelectric absorption and it is used only as a functional form to show that the average continuum of Compton-thick AGN is indeed very curved. Fig. 5 shows the average spectra of unabsorbed, absorbed and Compton-thick AGN and compares it to the general shape of the Cosmic X-ray Background (Ajello et al. 2008b).

The peak of the stacked spectrum of Compton-thick AGN (at z≈0) is at almost twice the energy of the peak of the CXB (see Fig. 5), testifying that if Compton-thick AGN are responsible for part of the emission at the peak of the CXB then the bulk of the population should be at z≈ 1. This seems to be in agreement with the prediction of population synthesis models (e.g. Gilli et al. 2007; Treister et al. 2009).

We also adopt a different strategy to check the results of the analysis of the stacked spectrum of the Compton-thick AGN. Instead of producing a stacked spectrum, we performed a simultaneous fit to the 9 spectra. In doing this we use the same baseline model for all the spectra (e.g. a power law or an absorbed power law) with a free normalization constant as to take into account the different source fluxes. As a first test, we tried as before a fit with a simple power-law model. This fit yields a photon index of 1.94±0.07 (in reasonable agreement with what found before) and a χ^2/dof=148.1/98. We then tried fitting with an absorbed power-law model. The improvement in the fit, with respect to the previous one, is very large (e.g. χ^2/dof =118.6/97) and the F-test confirms that the probability of obtaining such improvement by chance is $\sim 4 \times 10^{-6}$. The best-fit photon index is $2.29^{+0.15}_{-0.14}$ and the column density is $2.4^{+1.0}_{-0.8} \times 10^{24}\,\mathrm{cm}^{-2}$. A fit with a cut-off absorbed power law model (with the photon index set to 1.8 as before) produces a slight improvement (e.g. $\chi^2 = dof$=113.1/97) yielding an absorbing column density of $1.8^{+0.8}_{-0.3} \times 10^{24}\,\mathrm{cm}^{-2}$ and cut-off energy of 128^{+63}_{-34} keV. Within the statistical uncertainties, the results of this new analysis appear to be consistent with the results of the analysis of the stacked spectrum.

Our next step was then to fit the stacked spectrum of Compton-thick AGN with a more physical model. In this case we adopted an improved version of the model of Yaqoob (1997) which fully treats relativistic Compton scattering, i.e. the MYTorus model by Murphy & Yaqoob (2009) and Yaqoob et al. (2010)[2]. This model provides tables for the attenuation of the continuum emission (transmitted through the torus) and the scattered component computed via Monte Carlo simulations (a similar model can be also found in Matt et al. 1999). In principle both the transmitted and the scattered components should be fitted to the spectrum to ensure self-consistency of the model. In practice, because of the many model parameters and the limited energy bandpass of BAT, a fit with both compo-

[2]The model is available at www.mytorus.com

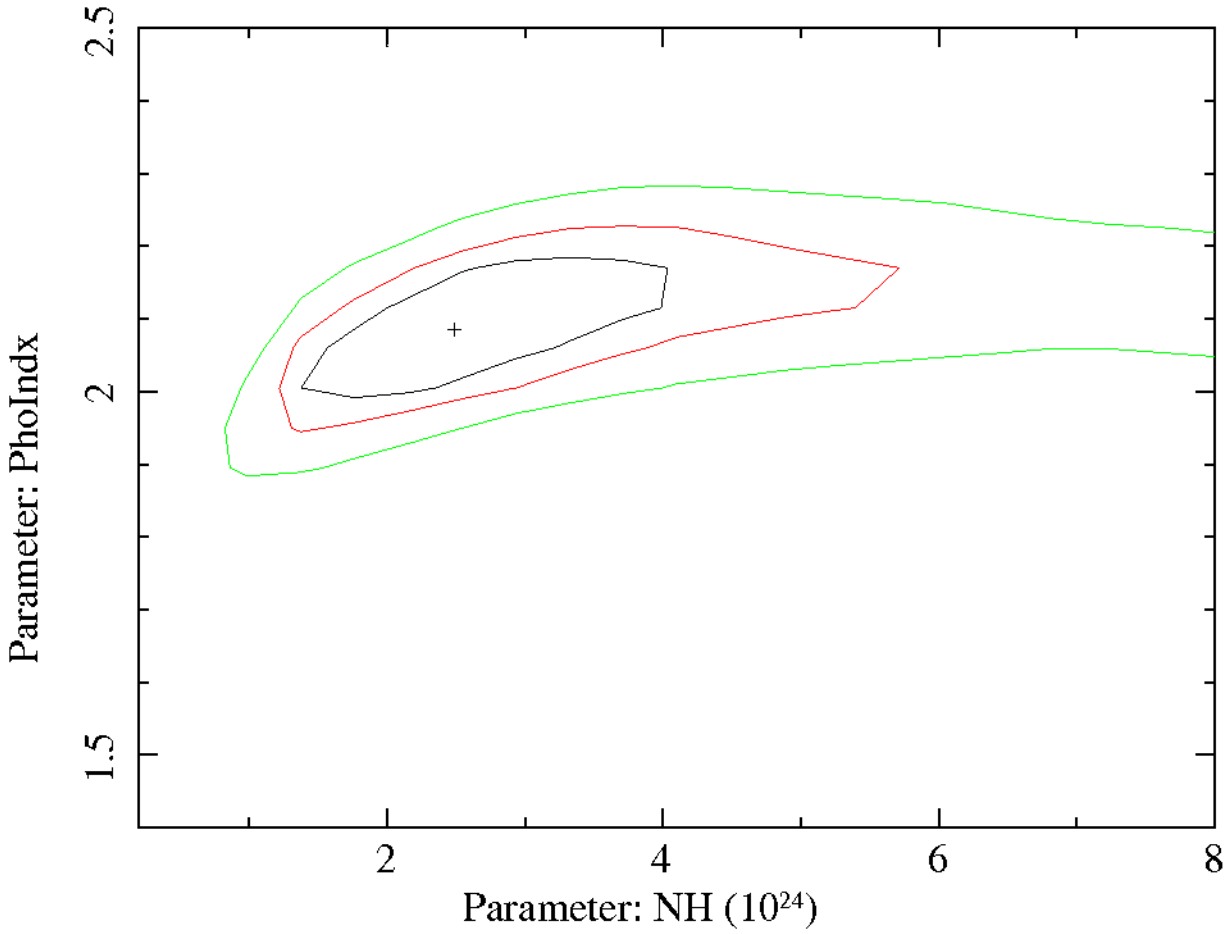

Fig. 6.— Confidence contours (1, 2, and 3 σ) for the photon index and the absorbing column density of the MYTorus model fitted simultaneously to all the 9 Compton-thick AGN spectra.

nents was not successful (e.g. $\chi^2/dof > 3$). However in this first exercise the normalization of the scattered component was a factor > 10 larger then the transmitted one. We then tried to fit the two components separately to understand whether one component is dominating over the other one. The best fit using the transmitted components yields a χ^2/dof=20.6/9 and is still thus a fairly poor fit. Instead we achieved a good fit (χ^2/dof=11.3/9) using the scattered component alone and an orientation of the torus (with respect our line of sight) of 60 degrees. The best-fit photon index is $2.17^{+0.10}_{-0.11}$ while the absorbing column density is $N_H = 3.7^{+2.1}_{-1.9} \times 10^{24}\, cm^{-2}$. We also attempt a simultaneous fit with the MYTorus model to all the 9 Compton-thick AGN spectra, leaving the normalization of each spectrum to be a free parameter of the fit. Again it appears that the scattered component is dominating over the transmitted one. Indeed we achieve a good fit to the data using the scattered component alone (e.g. χ^2 =111.1/97) and an inclination of the torus of $\sim$60 degrees. The best fit photon index is 2.08$\pm$0.10 and the absorbing column density is $2.5^{+1.8}_{-1.2} \times 10^{24}\,\mathrm{cm}^{-2}$. Fig. 6 shows the confidence contours of these two parameters. If we remove the most obscured AGN from the fit (i.e. NGC 1068) the index and N_H become respectively 2.05$\pm$0.10 and $2.7^{+2.2}_{-1.3} \times 10^{24}\,\mathrm{cm}^{-2}$ showing that our results are not driven by just one particular source.

From the best fit using the MYTorus model (either to stacked spectrum or the simultaneous fit) we derive that only $\sim$30 % of the intrinsic nuclear flux is observed in the 15–155 keV band. Finally, we note that the results presented in this section do not change if we remove the two brightest objects in the CT sample, nor if we remove the most absorbed source (e.g. NGC 1068, see above) from the sample. Nevertheless, given the paucity of CT AGN in our sample and the fact that they span one dex in absorbing column density, the results of this section must be taken with care as they might turn out not to be representative of the entire population of CT AGN.

3.2. Luminosity distribution and spectral properties

Luminosities of the Compton-thin AGN have been calculated through Eq. 2, therefore without taking absorption into consideration. We also tested whether the modeling of absorption introduced a bias in the distributions, even in the hard band sampled by BAT. To this aim we fitted all the sources with $\log N_H > 23.5$ taking Compton scatter into consideration (i.e. we used `cabs*zwabs*pow` in *Xspec*) and compared the resulting de-absorbed flux distribution with the one tabulated at the end of the paper. The `cabs` model has nonetheless some caveats that should be stated clearly: it assumes a constant Compton cross section equal to the Thomson one, so that it fails in describing the spectral hardening of the transmitted component due to the decay with energy of the Klein-Nishina cross section. Therefore

is typically used for spectra in the 2–10 keV energy band. Moreover, it does not take into account scattering from material out of the line-of-sight. The KS null probability (0.6) shows that indeed no appreciable difference is introduced by using a simple model for Compton-thin sources. As for the 9 Compton-thick objects, the fluxes have been de-absorbed as described in detail in §4.2. Fig. 7 shows the distribution of luminosity in the energy range 15–55 keV for the complete sample of AGN along with the distributions for the absorbed and unabsorbed AGN. The median values of the two subclasses read a logarithmic value of 43.2 and 43.8, respectively. A Kolmogorov-Smirnov test between these two populations reads a null hypothesis probability of 6.6×10^{-5}, if we neglect those producing the peak at $\log N_H$=20 in Fig. 10. The distance between the two populations is exacerbated when taking into account all the sources with $\log N_H$=20, since the KS probability drops to $\sim 10^{-9}$. Hence already by comparing the luminosity distributions there is evidence that the two populations are unlikely belonging to the same parent population, and this difference is independent from the modeling of absorption. This behavior is further discussed in detail in §6, where the X-ray luminosity functions of the two AGN classes are derived.

Photon index vs. Luminosity – In general, a correlation between the photon index and the accretion rate (expressed as the ratio of the bolometric luminosity and the Eddington luminosity) has been confirmed in numerous studies (see Ishibashi & Courvoisier 2010, and references therein). The general interpretation is that higher accretion rates lead to an increase in the photon density above the disk. This implies in general a more efficient cooling, and consequently steeper spectra. In this section we test whether the hard X-ray power law index is correlated with the luminosity in the BAT range, even if we are aware that the hard X-ray luminosity alone is an inaccurate proxy of the accretion rate. As it can be seen in Fig. 8 there is no indication that luminosity and photon index are correlated, confirmed by the Spearman's rank coefficient and null hypothesis probability respectively equal to 0.19 and ∼0.01. This might be produced by the fact that the objects in our sample have a broad distribution of black hole masses (and Eddington ratios[3]). Winter et al. (2009a) recently showed the absence (in the local BAT-selected AGN sample) on average, of this correlation between the 2–10 keV de-absorbed luminosities and Γ, as well as between a proxy of the Eddington ratio and the spectral index. The correlation between the 2–10 keV photon index and the luminosity was found not to be significant in many papers (Reeves & Turner 2000; Bianchi et al. 2009a), and the significance is generally low also in the works where it is claimed as real (Dai et al. 2004; Saez et al. 2008). It is worth noting that Winter et al.

[3]By definition $\lambda_{Edd} \equiv L_{Bol}/L_{Edd}$ and $L_{Edd} \equiv 4\pi GcMm_p/\sigma_T$, G and c being the gravitational constant and the speed of light, M and m_p the mass of the black hole and of the proton, σ_T the Thompson cross section.

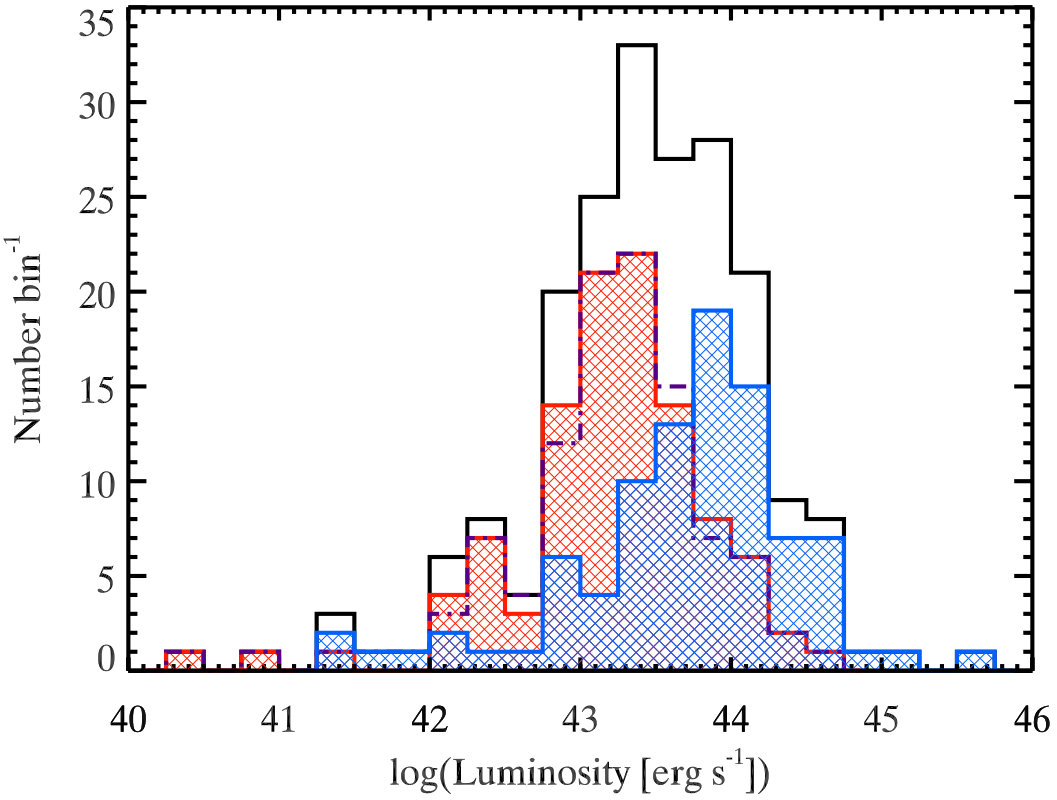

Fig. 7.— Luminosity distribution in the 15–55 keV energy range for the complete catalogue (grey) and for the absorbed sources (i.e. log $N_H \geq 22$, red). We also show (blue) the distribution for the sources with $\log N_H < 22$. The purple line shows the luminosity distribution of the absorbed sources without correction for absorption.

(2008) reported a positive correlation between the photon index and the 2–10 keV flux of individual sources, i.e. at high fluxes the sources tend to show steeper spectra. Interestingly, *Swift*–BAT beamed AGN (Fig. 2 in Ghisellini et al. 2010; Ajello et al. 2009b) do show a rather remarkable relation between the 15–55 keV luminosity and the spectral index. This relation is even stronger when looking at samples selected in the *Fermi*/LAT energy range. Nonetheless, the reason of the absence of this correlation in the objects of our sample is beyond the aims of this work.

Hard X-ray flux versus Absorbing column density – Fig. 9 shows the distribution of the sources in the flux–N_H plane. The absence of objects under $\sim 7 \times 10^{-12}$ erg cm^{-2} s^{-1} (which is represented by the horizontal line) reflects the sensitivity of *Swift*–BAT in the energy range

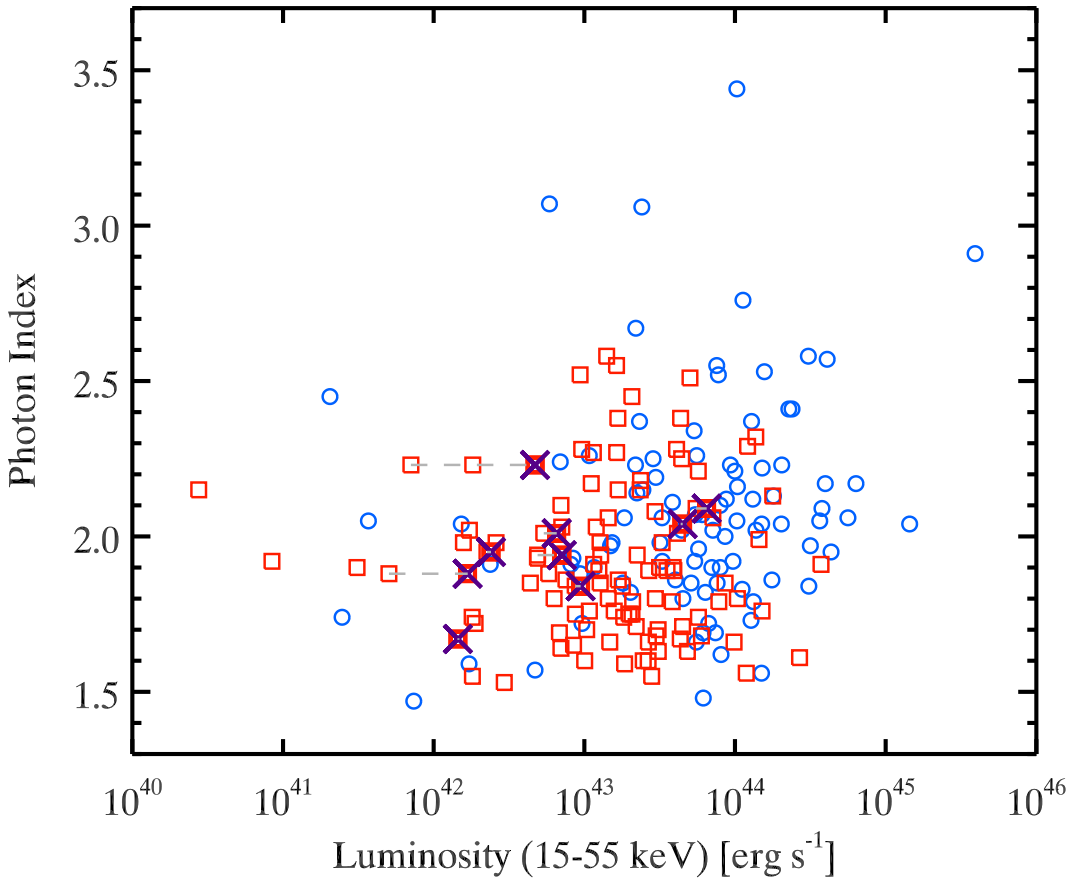

Fig. 8.— Photon spectral index resulting from the simple power law fit as a function of the BAT luminosity in the 15–55 keV range. The unabsorbed sources are shown with blue circles, while the absorbed sources are shown in red squares. The 9 Compton-thick sources are highlighted with crosses, and their de-absorbed luminosity is connected to the absorbed one by horizontal lines.

we selected. Indeed we see no correlation between these two parameters (Spearman's rank coefficient 0.04, and null hypothesis probability $P = 0.64$). Note that the absence of sources at small N_H and high fluxes, i.e. the top left region of the plot, reflects the tendency of the more luminous sources (which are intrinsically less numerous) of being unabsorbed. Indeed we showed in Fig. 1 that at a higher flux the sources are typically absorbed by columns in excess of 10^{22}. This explains the handful bright objects, i.e. with $F_X > 10^{-10}$ erg cm^{-2} s^{-1}, in the range 22 <logN_H< 23. We discuss in further detail the nine Compton-thick objects in §4.2.

4. Absorption in the local Universe

4.1. Observed N_H distribution

We derived the photoelectric absorption by the combined fit of the BAT spectra (averaged over 3 yrs.) and the available follow up observations in the 0.3–10 keV energy range (e.g. *XMM–Newton* or XRT). As described in §2.3 we adopted the value reported in the literature for $\sim 50\%$ of the sample, and the specific reference is reported in the table at the end of the paper. The absorption distribution is reported in Fig. 10. For 33 AGN (out of 197) the absorbing column density we measured was found to be consistent with (or smaller than) the Galactic absorption in the direction of the source. When we could not constrain the absorption or when its value was consistent with the Galactic one, we put the value logN_H=20, which in turn produced the high peak in the distribution in the bin 20<logN_H<20.5. Note that there are a handful of cases taken from the literature in which the column density is found to be lower than 10^{20} cm^{-2}.

When considering the whole AGN population we find that 53±4% ($1\,\sigma$ statistical error) are absorbed by column densities $\geq 10^{22}$ cm^{-2}. We find that the number of objects whose N_H is greater then 10^{24} cm^{-2} is 9/197. Thus the fraction of highly absorbed sources, know as Compton-thick AGN is $4.6^{+2.1}_{-1.5}$% ($1\,\sigma$ statistical error), all already known in the literature as extremely absorbed sources. These objects are highlighted in the table at the end of the paper. The fraction of Compton-thick sources at $\sim 10^{-11}$ erg cm^{-2} s^{-1} was predicted by population synthesis models to be, at the typical fluxes sampled by BAT in the range 7–15 % (see Comastri et al. 2009; Treister et al. 2009, and references therein).

An updated compilation of the most recent survey results in the hard X-ray band (e.g. above 10 keV) is reported in Tab. 2. It is clear that most, if not all, of these results indicate a lack of Compton-thick AGN if compared to the ∼30 % fraction found by Risaliti et al. (1999).

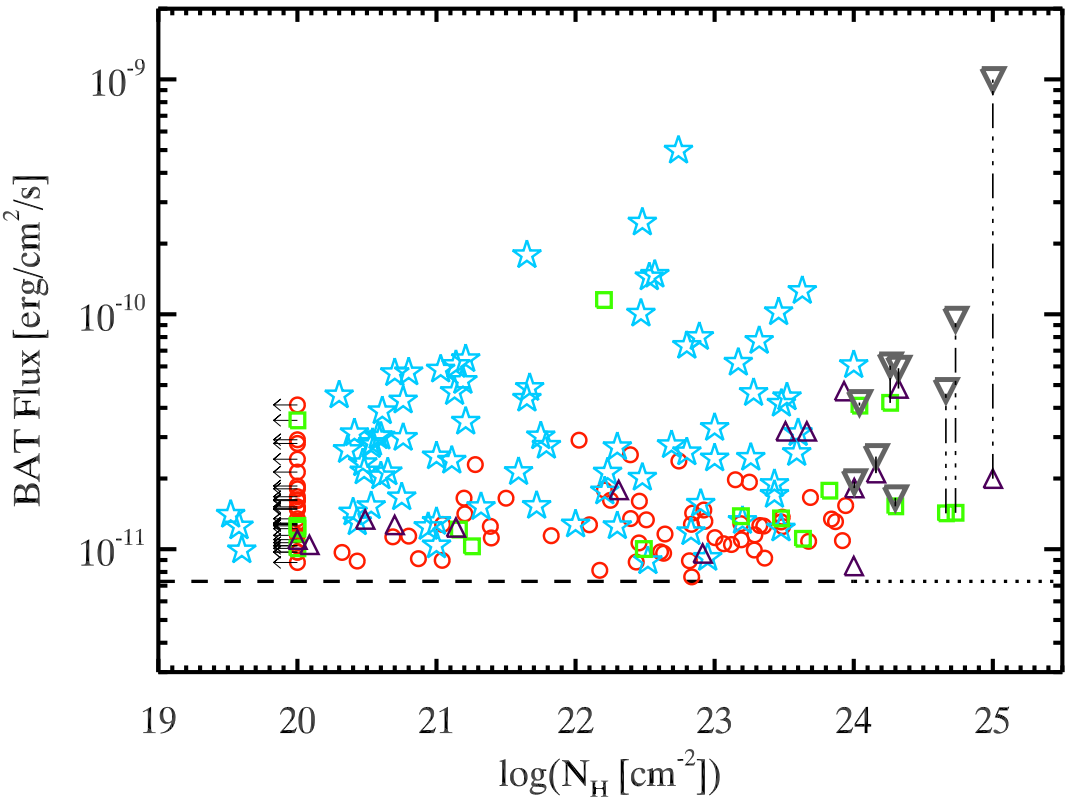

Fig. 9.— Scatter plot of the 15–55 keV fluxes of the sources *vs.* column density. Blue stars and purple triangles represent respectively the AGN already present in Tueller et al. (2008) and other references (see last table). Sources treated separately in this work are shown as red dots (follow up by *Swift*–XRT) and green squares (follow up by *XMM–Newton*). The horizontal dashed line represents the sensitivity limit of the 3-year survey (note that we draw a dotted line in the CT regime, where also BAT is biased, as discussed in § 4.2). Absorbed and un-absorbed fluxes (connected by vertical dash-dotted lines) are drawn for the 9 Compton-thick sources.

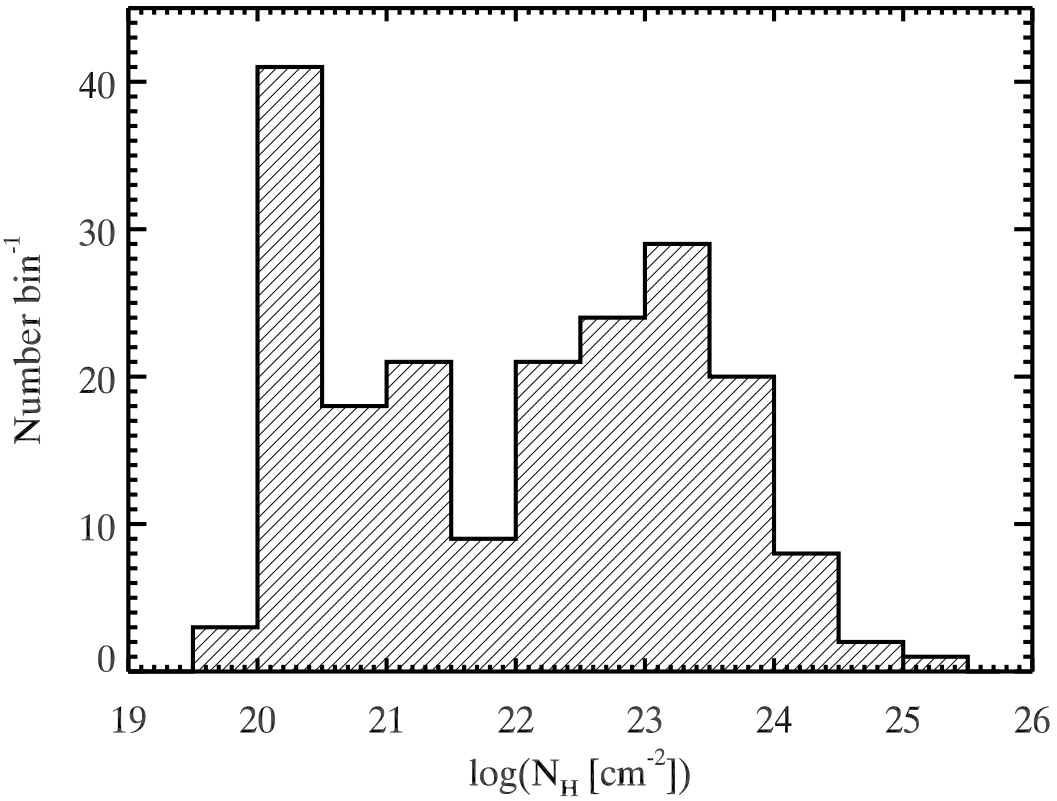

Fig. 10.— Observed column density distribution. The peak at $\log N_H = 20$ is produced by the sources for which absorption was negligible (of the same order of the galactic one).

Table 2: Observed fraction of absorbed and Compton-thick AGN, relative to the whole population for different X-ray surveys.

Reference	# Obj	Completeness	% Absorbed	% C-thick	Band (keV)	Instrument
Markwardt et al., 2005	54	95 %	$\sim$ 64%	$\sim$10%	15–200	*Swift*–BAT
Beckmann et al., 2006	36[a]	100 %	$\sim$ 64%	$\sim$ 10%	20–40	INTEGRAL
Bassani et al., 2006	56[b]	77 %	$\sim$ 65%	$\sim$ 14%	20–100	INTEGRAL
Sazonov et al., 2007	91	93 %	$\sim$ 50%	$\sim$ 10-15%	17–60	INTEGRAL
Ajello et al., 2008a	24	100 %	$\sim$ 55%	<20 %	14–170	*Swift*–BAT
Tueller et al., 2008	103	100 %	$\sim$ 50%	$\sim$ 5%	14–195	*Swift*–BAT
Paltani et al., 2008	34[c]	100 %	$\sim$ 60%	<24 %	20–60	INTEGRAL
Della Ceca et al., 2008	62	97 %	$\sim$ 57%	0	4.5–7.5	*XMM–Newton*
Malizia et al., 2009	79[d]	100 %	$\sim$ 43%	7%	20–40	INTEGRAL
Beckmann et al., 2009	135[e]	$\sim$ 97 %	$\sim$ 44%	$\sim$4 %	18–60	INTEGRAL
This work	197	100 %	$\sim$ 53%	$4.6^{+2.1}_{-1.5}$ %	15–195	*Swift*–BAT

[a] The complete sample is 42 AGN, 36 of which are Seyfert galaxies.

[b] The complete sample is 62 AGN, 6 of which are Blazars and 14 are unindentified.

[c] Since the Paltani et al. sample may contain a fraction of spurious sources, we restricted their sample to a limiting significance of $6\,\sigma$. Above this threshold all sources are identified (see Tab. 2 in Paltani et al. 2008).

[d] There are 88 objects reported to be at significance $> 5.2\sigma$. 79 of those are Seyfert galaxies, the remaining being Blazars.

[e] The complete sample comprises 187 objects with $> 3\sigma$ significance in the 18–60 keV energy band. According to the authors (see Sect 4.1 in Beckmann et al. 2009) there are 135 Seyfert galaxies with measured absorption. Only 7/187 sources are listed generically as AGN without information on redshift.

4.2. The BAT bias and the intrinsic N_H distribution

BAT is the least biased X-ray instrument, particularly when comparing it to 2–10 keV telescopes, for the detection of obscured objects. Nonetheless, even in the > 10 keV band a relevant fraction of the source flux might be lost if the source is Compton-thick. In order to show this effect we computed the ratio between the observed and the intrinsic nuclear flux of an AGN for increasing column densities. In this exercise, we took both photoelectric absorption and Compton scattering into account using MYTorus. The nuclear, intrinsic, emission has been modeled as a power law with a photon index of 1.9. The results are shown in Fig. 11. From this plot it is apparent that the BAT survey is unbiased up to $\log N_H \approx 24$ and then becomes biased against the detection of Compton-thick objects. Furthermore, the absorption bias affects much more severely the 2-10 keV band already for $\log N_H \geq 23$ (see same Fig. 11).

We also performed joint spectral fits of *XMM–Newton* and *Swift*–BAT data for all the Compton-thick objects in our sample to determine the fraction of the intrinsic flux which is seen in the 15-55 keV band. The details of this analysis will be reported in a future

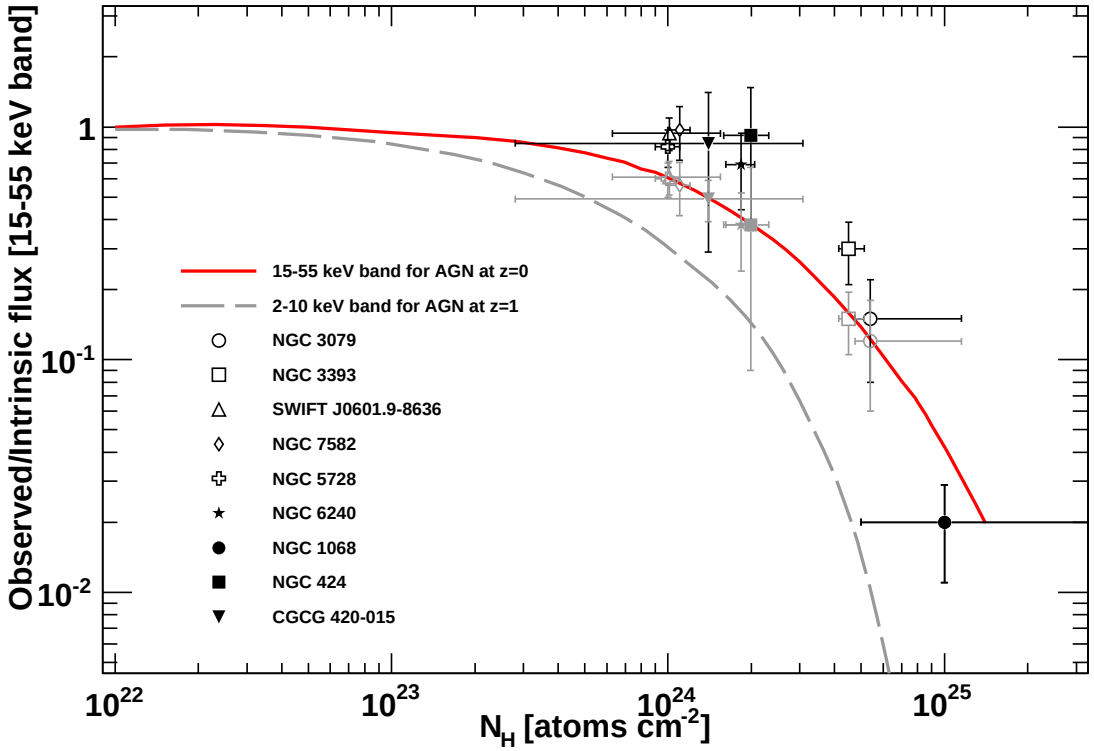

Fig. 11.— Ratio of observed to intrinsic nuclear flux for an AGN, with a power-law spectrum with index of 1.9, as a function of the column density of the torus as seen edge-on. The red solid line shows the ratio for the 15-55 keV band for an AGN in the local Universe (e.g. the typical case for the BAT survey). The dashed line shows the ratio for the 2-10 keV band for an AGN at redshift ~ 1, i.e. the typical redshift for AGN detected in the *XMM–Newton*/Chandra surveys (see e.g. Akylas et al. 2006). Note that the BAT survey is unbiased (e.g. ratio $\approx$1) for $\log N_H \leq 23.5$. The black data points show the ratio of observed to intrinsic flux estimated for the BAT Compton-thick AGN taking into account only photoelectric absorption. The gray data points show the ratio also when Compton scattering is fully taken into account.

publication (Burlon et al. in preparation), however the results are summarized in Tab. 3 and in Fig. 11. Only for SWIFT J0601.9-8636, NGC 5728, CGCG 420-015, and NGC 1068 we used the values available in the literature. Indeed, *XMM–Newton* data are not available for SWIFT J0601.9-8636 and NGC 5728, so we used the values derived with Suzaku by Ueda et al. (2007) and Comastri et al. (2010), respectively. NGC 7582 was largely discussed in Piconcelli et al. (2007) and Bianchi et al. (2009b), as for the variations of a factor ~ 2 in

the thicker absorber. We used the *XMM–Newton* observation taken in 2005, and therefore tagged this object as Compton-Thick. Variations of the thick absorber can in principle take place for other sources as well, altering the fraction of CT objects according to the observation used for the analysis. The Compton-thick nature of CGCG 420-015 (aka IRAS 04507+0358) was discovered by Severgnini et al. (2010). It was known to be a highly absorbed Sy2 galaxy, but with the use of deep (100 ks) Suzaku observations, in addition to the ones available, the authors found N_H to be $\sim 1.3 - 1.5 \times 10^{24}$ cm^{-2}, with minor variations according to the model used to fit the combined spectra. NGC 1068 is a complex object which has been analyzed in detail in the past. According to Matt et al. (2004), the nuclear emission is completely suppressed and the source is seen only in reflected light. The column density is probably in excess of 10^{25} atoms cm^{-2} (Matt et al. 2004) and the reflection component is of the order of a *few* % of the nuclear flux (Iwasawa et al. 1997). For these reasons the position on the plot of NGC 1068 should be considered tentative. Fig. 11 also shows the difference in the observed-to-intrinsic flux ratio when also Compton scattering is taken into account (using the MYTorus model). Note however that modeling with MYTorus contains an implicit assumption, i.e. that the scattering material has a toroidal geometry with given parameters (half-opening angle of 60°, corresponding to a covering factor of $\Delta\Omega/4\pi = 0.5$). The line-of-sight of the observer is a fixed parameter of the fit.

It is interesting to note that there is relatively good agreement between the model line and the observations of single Compton-thick objects detected in the *Swift*–BAT survey. In Fig. 9 we showed the fluxes of the 9 Compton-thick AGN, before and after the correction for the missed flux, connected by dash-dotted lines. The horizontal line representing the limiting flux of the survey was turned into a dotted line to visually indicate the increasing bias in the CT regime.

Table 3: Ratio of the observed flux with respect to the nuclear (unabsorbed) flux in the 15–55 keV band for the 9 Compton-thick objects in the sample. Errors are quoted at 90 % CL. Four sources were fitted using *XMM–Newton* and *Swift*–BAT. For the remaining objects we used values from the literature.

Source	F_{obs}/F_{nucl}	Error	N_H (10^{24} cm^{-2})	N_H error (10^{24} cm^{-2})
NGC 3079	0.15	0.07	5.40	(-0.65,6.10)
NGC 3393	0.30	0.10	4.50	(-0.36,0.62)
SWIFT J0601.9-8636 [a]	0.94	0.15	1.01	(-0.38,0.54)
NGC7582	0.97	0.25	1.10	(-0.05,0.05)
NGC 5728 [b]	0.82	0.15	1.0	(-0.1,0.1)
NGC 6240	0.69	0.25	1.83	(-0.23,0.22)
NGC 1068 [c]	0.02	0.01	>10	(-5, >10)
NGC 424	0.92	0.56	1.99	(-0.40,0.32)
CGCG 420-015 [d]	0.85	∼0.20	1.46	(-0.11,0.07)

[a] Ueda et al. (2007) [b] Comastri et al. (2010) [c] Matt et al. (2004) and Iwasawa et al. (1997) [d] Severgnini et al. (2010)

Essentially the absorption bias limits the detection of Compton-thick objects only to those with bright (intrinsic) fluxes and in the very local Universe. Indeed three of the most famous Compton-thick objects (NGC 1068, NGC 4945 and the Circinus galaxy) are also among the closest known AGN. Thus the distribution reported in Fig. 10 compares sources detected at different limiting *intrinsic* fluxes. It is possible to correct for this effect by taking into account the selection effect due to the large column density. The *intrinsic* absorption distribution can be expressed as:

$$\frac{dN}{dLogN_{\rm H}} = \int_{S_{min}}^{S_{max}} \frac{dN}{dS}(N_{\rm H})\ dS, \tag{3}$$

where the $\mathrm{d}N/\mathrm{dLogN_H}$ is in unit of sr^{-1} per logarithmic bin of $\mathrm{N_H}$, S is the observed source flux, and $\mathrm{d}N/\mathrm{d}S(\mathrm{N_H})$ is the log$N$–log$S$ of sources in a given $\mathrm{logN_H}$ bin. The minimum *observed* flux (S_{min}) of integration should be set so that the limiting *intrinsic* flux is the same for all the bins. In this way the absorption distribution derived is representative of the density of sources at the same limiting intrinsic flux.

The relationship between observed and intrinsic flux can be expressed as $S^{obs} = K(N_{\rm H})\ S^{intr}$ where $K(N_{\rm H})$ is the ratio plotted in Fig. 11. Thus S_{min} can be set to $10^{-11} \times K(N_{\rm H})$ to produce a uniform absorption distribution for sources with an intrinsic flux greater than 10^{-11} erg cm^{-2} s^{-1}. Eq. 3 can thus be rewritten as:

$$\frac{dN}{dLogN_{\rm H}} = \frac{A(N_H)}{1-\alpha}\left[S_{max}^{1-\alpha} - (10^{-11}K(N_{\rm H}))^{1-\alpha}\right] \quad , \tag{4}$$

where $A(N_{\rm H})$ and α are the normalization and the index of the *log* N–*log* S in a given $\mathrm{logN_H}$ bin. Here we assumed that the source count distribution can be approximated with a power-law function (e.g. $dN/dS = AS^{-\alpha}$). This assumption is well justified by the fact that the source count distribution of the entire BAT sample is well represented by a single power law (e.g. see Ajello et al. 2009b) and that the source count distribution of AGN shows a break at much lower fluxes (e.g. Cappelluti et al. 2007). In order to derive the intrinsic absorption distribution we used 0.25 dex $\mathrm{logN_H}$ bins. For each bin, a source count distribution has been constructed and a power law has been fitted to it employing a Maximum Likelihood algorithm. This power law was then used to estimate the density of objects (per steradian) in a given $\mathrm{logN_H}$ bin (i.e. Eq. 4). All the power-law indices were found to be compatible with a Euclidean index (i.e. 2.5 for a differential distribution). The index α has been fixed to 2.5 for all those bins with less than 5 objects. We checked that fixing the index to 2.5 for all bins or allowing it to vary does not change the results presented here. For each $\mathrm{logN_H}$ bin the error on the density of sources is derived from the Poisson error on the number of sources present in that bin to preserve the original counting statistics.

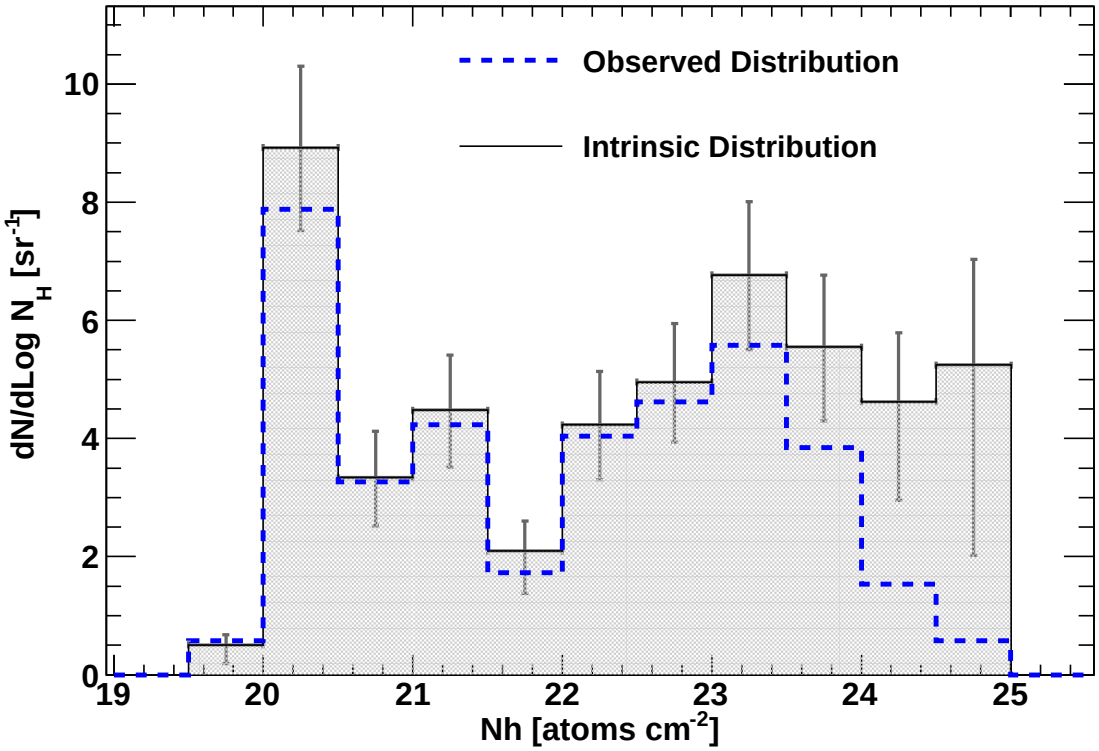

Fig. 12.— Intrinsic absorption distribution compared to the observed one (dashed line). Errors bars are derived from counting statistics in each bin.

The intrinsic absorption distribution is shown in Fig. 12. From this we derive that the *intrinsic* fraction of Compton-thick sources ($\log N_H > 24$) is 20^{+9}_{-6} %, where the error is only statistical. It is apparent that the observed distribution starts to deviate from the observed one only for $\log N_H \geq 23.5$. We also derive that the *intrinsic* fraction of absorbed sources is 65 ± 4 %. A systematic error in estimating the *intrinsic* fraction of Compton-thick sources might arise from both the power-law indices fitted in Eq. 4 and from the $K(N_{\rm H})$ correction factor (e.g. the curve plotted in Fig. 11). Fixing all the α parameters to 2.5 or allowing all of them to vary changes the above fraction of about 1 %. Thus the exact shape of the $\log N$–$\log S$ in each $\log N_{\rm H}$ bin does not contribute a large systematic error.

On the other hand, the knowledge of the fraction of transmitted flux (e.g. $K(N_{\rm H})$ and Fig. 11) plays a major role in the derivation of the density of Compton-thick AGN. The angle at which our line-of-sight intersects the torus and the power-law index of the intrinsic AGN spectrum can modify the fraction of Compton-thick AGN. Playing with these different parameters we derive that the systematic uncertainty on the fraction of Compton-thick AGN

is $\sim$5 %.

Also Malizia et al. (2009), using INTEGRAL, showed that the fraction of Compton-thick AGN is likely larger than the observed $\sim$5 %. Instead of correcting for the missing population, they adopt a redshift cut (z$\leq$0.015) which would ensure, according to the authors, to have a complete sample. In their sample of 25 AGN, they found 6 Compton-thick AGN, thus the fraction of Compton-thick AGN is 24^{+11}_{-9} % of the total population in agreement with our estimate.

As visible from Fig. 11, there is also a slight overestimate (although compatible within $1\,\sigma$ with the observed density) of the intrinsic density of objects with Log$N_H \approx 20$. This is due to the fact that a few objects in that bin have actually a lower column density that could not be effectively constrained in the 0.3–10 keV energy band. For all those objects the Log$N_H \sim 20$ can be considered an upper limit to the true absorbing column density. Because of this, the source count distribution in the Log$N_H \approx 20$ bin tends to overestimate the true intrinsic density. However, as seen in the Fig. 11 this effect is small.

5. Anti-correlation of Absorption and Luminosity

According to the AGN unified model (Antonucci 1993; Urry & Padovani 1995) all the different properties of AGN can be ascribed solely to orientation effect. Thus one should not observe variations of any other property with e.g. luminosity, accretion rate and redshift. However, already 30 years ago, Lawrence & Elvis (1982) reported the discovery of the anti-correlation of the fraction ($F_{\%}$) of obscured AGN (relative to the whole population) and luminosity. More recently different authors addressed the same issues with contradicting results. For example some studies (e.g. Treister & Urry 2006; La Franca et al. 2005; Della Ceca et al. 2008; Winter et al. 2009a; Brusa et al. 2010) suggest that $F_{\%}$ decreases with X-ray luminosity, while Dwelly & Page (2006) point to $F_{\%}$ being independent of L_X. Also Sazonov & Revnivtsev (2004), Sazonov et al. (2007), and Beckmann et al. (2009) pointed out that an anti-correlation of the fraction of absorbed sources and X-ray luminosity seems to exist.

Fig. 13 shows how the fraction of obscured AGN (those with log$N_H \geq 22$) changes as a function of X-ray luminosity (in the 15–55 keV band) in our survey. The width of each bin has been chosen so that the number of object per bin is constant ($\sim$ 33). The errors on the number of absorbed sources and the total number of sources per bin have been propagated with the recipes for Binomial statistics (see Gehrels 1986, in particular Tab. 6). Binomial statistics apply specifically when dealing with ratios of small numbers. The data

are correlated, as the Spearman's rank correlation coefficient is r_s = -0.94. The probability of a chance correlation (4.8×10^{-3}) shows that the correlation is true at the 2.9σ confidence level.

We also show for comparison the INTEGRAL results of Beckmann et al. (2009), by converting the INTEGRAL 20–100 keV luminosities into 15–55 keV luminosities and selecting only non-blazar sources with z<0.3. The two data-sets are in reasonable agreement although the lower fraction of absorbed AGN in the INTEGRAL sample (with respect to the BAT sample) might be ascribed to completeness issues of the former.

In the BAT sample, the absorbed AGN fraction displays a flattening in the low luminosity regime, and the correlation becomes clearly non-linear ($\chi^2/dof \gtrsim 3.5$). Thus, we tried to fit the fraction of absorbed AGN with the empirical function proposed by Gilli et al. (2007) of the form:

$$F_{\%}(L_X) = R_{low} e^{(-L_X/L_C)} + R_{high}[1 - e^{(-L_X/L_C)}] \quad (5)$$

where R_{low} is the low luminosity asymptotic behavior, R_{high} the high luminosity one, and L_C is a "critical" luminosity at which the drop occurs. We fitted this function to the data: the best fit values for R_{low}, R_{high}, and $\log(L_C)$ are respectively 0.8, 0.2, and 43.7. This fit yields a $\chi^2/dof = 1.3$ which shows that this fit is better than a simple linear relation between the obscured AGN fraction and (the logarithm of) luminosity. This result will be discussed in details in in § 6.

In the literature (e.g. Hasinger 2008; Della Ceca et al. 2008) the minimum luminosity considered for an AGN in the 2–10 keV energy range, was typically greater than 10^{42} erg s^{-1}. Since the low luminosity tail of our distribution (see Fig. 7) extends to $\sim 2.8 \times 10^{40}$ erg s^{-1} we checked, for the sake of completeness, if by introducing a cut at 10^{42} erg s^{-1}, changed our findings. When transforming the 2–10 keV luminosity of 10^{42} erg s^{-1} to the 15–55 keV band, we find that only 7 sources fall below this limiting luminosity. The level of correlation of the data remains unchanged, while instead the χ^2/dof value for a linear fit, decreases to ~ 1.8. These results are shown in Fig. 13 (b). It is still apparent that the linear fit (which shows a slope of -0.26 ± 0.05) is not a good representation of the data since the first bin and the last two show a flattening of the fraction of absorbed AGN. Finally, it is worth considering that (i) the contribution from the stellar population hardly extends above $\sim 10^{41}$ erg s^{-1} (Ranalli et al. 2003; Norman et al. 2004), and (ii) in the 15–55 keV band this contribution is expected to decrease to even a lower fraction of the "bolometric" luminosity (see e.g. Voss & Ajello 2010).

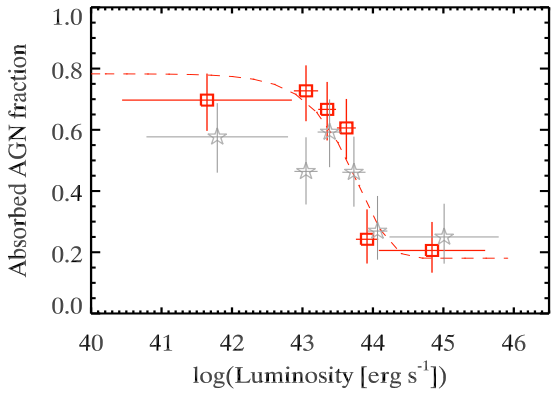

(a) The red dashed line represent the fit with Eq. 5. Grey stars represent, for comparison, data from Beckmann et al. (2009). Luminosities measured by INTEGRAL have been converted into the 15–55 keV energy range.

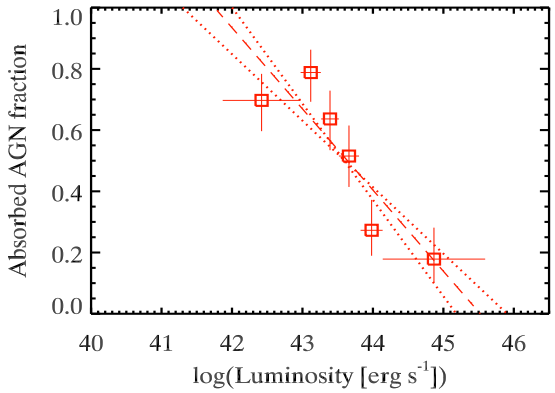

(b) Same as above (a) but with a cut in luminosity, as discussed in the text. The dashed (dotted) line represents a linear fit to the data (1σ uncertainties).

Fig. 13.— Fraction of the obscured (i.e. $N_H \geq 10^{22}$ cm^{-2}) AGN as a function of 15–55 keV luminosity (red squares). The data have been grouped such as to have an equal number of sources per luminosity bin. Errors on fraction of absorbed AGN have been computed using Binomial statistics (see Gehrels 1986) and are drawn at $1\,\sigma$ level.

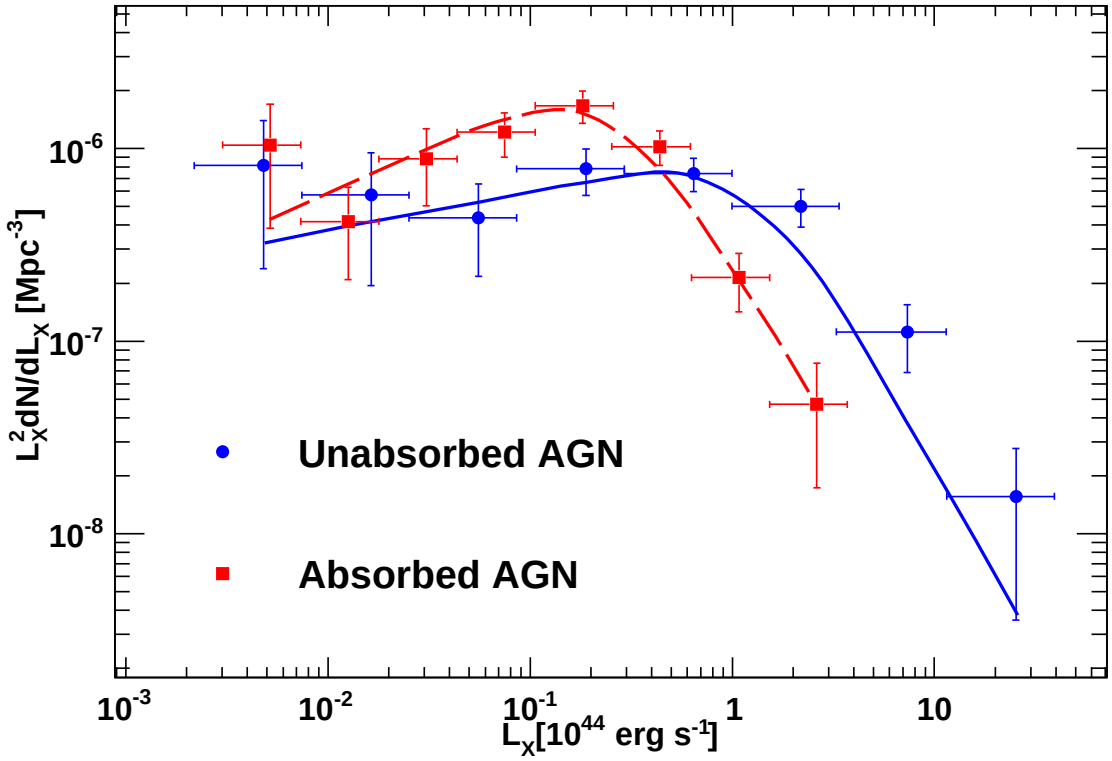

Fig. 14.— Luminosity function of absorbed ($\log N_H \geq 22$, squares) and unabsorbed AGN ($\log N_H < 22$, circles) with the respective best-fit models (solid and dashed lines). The luminosity functions have been multiplied by L_X^2 to highlight the different positions of the break luminosities.

6. Luminosity Functions of AGN

We estimate the X-ray luminosity function (XLF) of AGN using the $1/V_{MAX}$ method (equivalent in our formalism to the $1/V_a$ method). In this framework the XLF can be expressed as:

$$\Phi(L_X, z) = \frac{dN}{dL_X} = \frac{1}{\Delta\ L_X}\ \sum_{i=1}^{N} \frac{1}{V_{MAX,i}} \tag{6}$$

where $V_{MAX,i}$ is the maximum comoving volume associated with the i_{th} source. This is defined as:

$$V = \int_{z=0}^{z=z_{MAX}} \frac{dV}{dz}\ \Omega(L_i, z) dz, \tag{7}$$

where dV/dz is the comoving volume element per unit redshift and unit solid angle (see e.g. Hogg 1999), z_{MAX} is the maximum redshift after which the sources would not be detected anymore in the BAT survey and $\Omega(L_i, z)$ is the sky coverage of the survey. The XLF of the two different classes of AGN, obscured and unobscured, is reported in Fig. 14.

We made a Maximum Likelihood fit to the two different datasets using a broken power-law of the form (see e.g. Ueda et al. 2003; Hasinger et al. 2005):

$$\Phi(L_X, z=0) = \frac{dN}{dL_X} = \frac{A}{ln(10) L_X} \left[\left(\frac{L_X}{L_*} \right)^{\gamma_1} + \left(\frac{L_X}{L_*} \right)^{\gamma_2} \right]^{-1} \tag{8}$$

The ML estimator can be expressed as:

$$\mathcal{L} = -2 \sum_i \ln \frac{\Phi(L_{X,i}, z_i) V(L_{X,i}, z_i)}{\int \Phi(L_X, z) V(L_X, z) dL_X}\ . \tag{9}$$

Table 4: Best-fit parameters of X-ray Luminosity Functions in the 15-55 keV band

SAMPLE	# Objects	Norm.[1]	L*[2]	γ_1	γ_2
ALL	199	1.53e-5	$0.53^{+0.15}_{-0.15}$	$0.74^{+0.07}_{-0.08}$	$2.60^{+0.19}_{-0.20}$
ABSORBED	105	2.59e-5	$0.26^{+0.08}_{-0.07}$	$0.58^{+0.12}_{-0.13}$	$2.75^{+0.34}_{-0.30}$
ABSORBED[3]	99	3.93e-5	$0.26^{+0.14}_{-0.09}$	$0.51^{+0.28}_{-0.34}$	$2.63^{+0.38}_{-0.31}$
UNABSORBED	92	1.90e-6	$1.34^{+0.48}_{-0.38}$	$0.80^{+0.11}_{-0.12}$	$2.88^{+0.37}_{-0.31}$

[1] Normalization of the XLF expressed in units of $\mathrm{erg^{-1}\,s\,Mpc^{-3}}$.

[2] In units of $10^{44}\,\mathrm{erg\ s^{-1}}$.

[3] *Intrinsic* XLF of absorbed AGN. The luminosity of the absorbed AGN with $\mathrm{LogN}_H \geq 23.5$ have been de-absorbed with the method described in § 4.2.

The best-fit parameters are obtained by minimizing $\mathcal{L}$. Their $1\,\sigma$ error are computed by varying the parameter of interest, while the others are allowed to float, until an increment of

$\Delta\mathcal{L}$=1 is achieved. This gives an estimate of the 68 % confidence region for the parameter of interest (Avni 1976). The likelihood function does not depend on the normalization A since it cancels out in Eq. 9. Once the slope α is determined, the normalization is derived as the value which reproduces the number of observed sources. An estimate of its statistical error is given by the Poisson error on the number of sources used to build the XLF.

The results of the ML fits to the XLFs of whole population of AGN and obscured and unobscured subclasses are summarized in Tab. 4. We focussed mainly on the difference between the two subsamples of absorbed and unabsorbed AGN, but we used the total XLF in Fig. 16 in order to account for the obscuration-luminosity relation. It is apparent that the XLFs of the two classes of objects are not the same. In particular the 'break' luminosity L^* is different at $\sim$2.8 σ level, with absorbed AGN having on average lower luminosity than unabsorbed ones. Also Della Ceca et al. (2008), analyzing a small sample of XMM-Newton AGN, found different XLFs for obscured and unobscured sources. However, in their case they cannot allow (presumably due to the low number of sources) L* to be a free parameter of the fit. In our case, this can be done and there is evidence (albeit marginal) that the typical luminosity of absorbed and unabsorbed AGN is different. The difference between the luminosity functions of absorbed and unabsorbed objects is however not a surprise. Indeed it is expected in view of the anti-correlation of the absorption fraction and luminosity (e.g. Fig. 13). The two luminosity function are equal at a luminosity of 4×10^{43} erg s^{-1}. This is exactly the luminosity at which the fraction of absorbed objects is 0.5 (see Fig. 13). For the very first time this trend is clearly seen in the luminosity function of absorbed and unabsorbed objects (as derived from the same energy band).

We tested if this 'trend' of the break luminosity holds for smaller subsamples, namely if the very most absorbed sources show a significantly smaller value of L^*. This exercise needs of course a sufficient number of sources per subsample, in order to constrain the parameters of the fit with the broken power law. Therefore we divided the parent population into four bins of absorption containing $\sim$ 50 sources each. For each of the subsamples we computed the best fit values of the XLF as described before. In Fig. 15 we showed the break luminosity (in units of 10^{44} erg cm^2 s^{-1}) versus N$_{\rm H}$. This exercise confirms, albeit with a statistical significant uncertainty, that absorbed AGN appear to be intrinsically less luminous than unabsorbed AGN. We also performed an additional test in order to exclude that this finding is partially driven by the bias against the detection of the most absorbed AGN. We computed the *intrinsic* XLF of absorbed AGN by de-absorbing the AGN luminosities using the model described in §4.2. As clearly seen from Fig. 12, this correction is negligible for all AGN with Log$N_{\rm H}\leq$23.5, modest for all those with 23.5 <Log$N_{\rm H}\leq$24 and relevant for AGN with Log$N_{\rm H}\geq$24. It has to be noted that the *intrinsic* XLF of absorbed AGN suffers from incompleteness at the lowest luminosities. Indeed, because of the effect of large absorption,

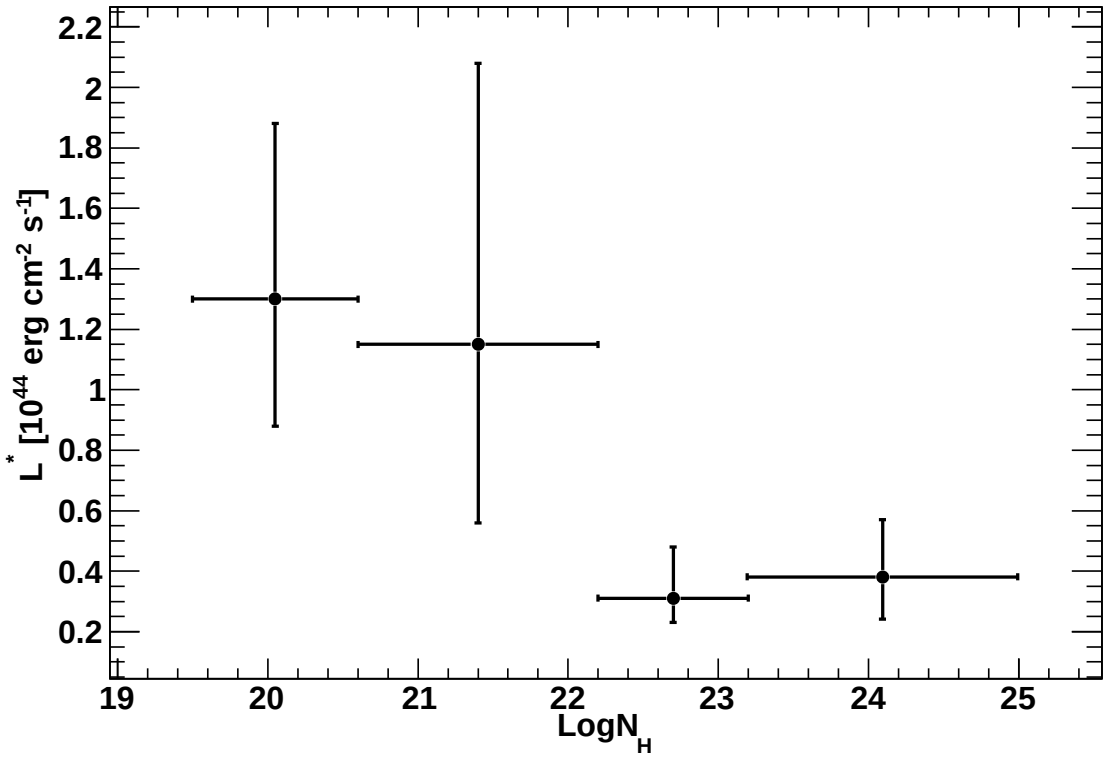

Fig. 15.— Break luminosity (L^*, as in Eq. 8) in units of 10^{44} erg cm^2 s^{-1}, versus column density. The sample was divided into four equally populated subsamples of $\sim$50 sources. Errors are quoted at $1\,\sigma$ level.

sources with an intrinsic luminosity large enough to be detected by BAT might be pushed below the BAT sensitivity. In order to avoid this problem we cut the sample at the minimum de-absorbed luminosity for which the $K(N_H)$ correction (discussed in §4.2) was less than 1. This minimum, de-absorbed, luminosity is 2×10^{42} erg s^{-1} and we consider the BAT sample to be complete above it. The parameters of the *intrinsic* XLF of absorbed AGN are reported in Tab. 4. It is clear that the *intrinsic* XLF of absorbed AGN is found to be in very good agreement with the XLF of absorbed AGN. This is because the bias against the detection of absorbed AGN is relevant only for $\mathrm{LogN_H}\geq 24$ and above this threshold the BAT sample contains very few objects.

Finally, we test whether the anti-correlation of the fraction of obscured AGN and luminosity (found in the previous section) can be reproduced by the two different XLFs for absorbed and unabsorbed AGN. To this extent we divide the XLF of absorbed AGN by the XLF of the entire sample. We computed the $1\,\sigma$ error on this function via bootstrap with replacement employing 1000 bootstrapped samples. In order not to suffer from biases derived from the detection of Compton-thick AGN and also to avoid the need of correcting for them, we also excluded all objects with $\mathrm{Log}N_H \geq 24$. As shown in the previous sections the BAT sample can be considered complete for all AGN with $\mathrm{Log}N_H \leq 24$. The results of our analysis are shown in Fig. 16 along with the observed anti-correlation of the obscured AGN fraction and luminosity. The agreement within errors is clear at all luminosities and the decreasing trend in the absorbed fraction at low luminosity does not depend on the presence or the absence of Compton-thick AGN. The trend of the fraction of obscured AGN and luminosity can be perfectly reproduced by the analysis of the XLFs of the absorbed and unabsorbed AGN. In turn, this difference can be ascribed to the fact that on average obscured AGN appear to be less luminous. Even more interestingly, the ratio of XLFs predicts (in agreement with the observations) that the fraction of obscured sources decreases at low luminosities (i.e. $L_X < 10^{42}$ erg s^{-1}). However, we caution the reader that, due to the lack of sources, the obscured AGN fraction is, at low-luminosities, compatible within $3\,\sigma$ with a constant fraction of $\sim 80\,\%$.

7. Discussion

7.1. Compton-thick AGN and the Cosmic X-ray Background

It is well understood that the shape and the intensity of the CXB cannot be reproduced successfully if Compton-thick AGN ($\mathrm{logN_H} \geq 24$) are not invoked. They are required to produce $\sim$10 % of the CXB intensity at $\sim$ 30 keV (Gilli et al. 2007; Treister et al. 2009). However, since the extreme absorption makes these objects faint at X-rays, Compton-thick

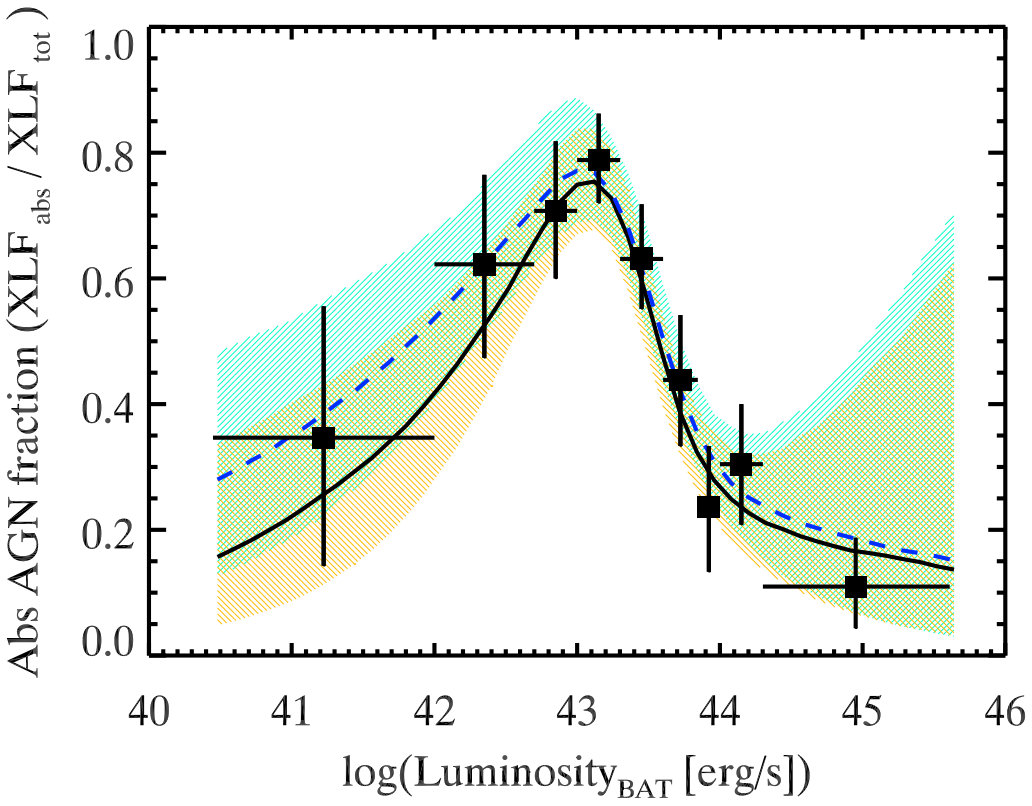

Fig. 16.— Fraction of the absorbed AGN versus luminosity in the 15–55 keV energy range. The lines are obtained by dividing the XLF of obscured AGN by the XLF of the whole population. The dashed (solid) line represents the whole sample (with a cut at 2×10^{42} erg s^{-1}). The shaded bands represent the $1\,\sigma$ uncertainty computed with a bootstrap analysis, blue for the whole sample and yellow for the sample with the cut in luminosity.

AGN have to be numerous (e.g. ∼30 % of the whole AGN population) in order to fulfill the above requirement. Despite this general belief, all searches of Compton-thick AGN have so far highlighted a lack of Compton-thick AGN (see Tab. 2). This work, which uses the largest AGN sample collected so far above 15 keV, shows that the *detected* fraction of Compton-thick AGN is only $4.6^{+2.1}_{-1.5}$ %. At the fluxes currently sampled by *Swift*–BAT population synthesis models predict this fraction to be either ∼16% if one adopts the Gilli et al. (2007) or ∼8% the Treister et al. (2009) model. Thus our measurement appears to be substantially lower than both predictions, but compatible within $\sim 2\,\sigma$ with what reported by Treister et al. (2009).

However, one must take into account that even X-rays with energies larger than 15 keV are absorbed if the source is mildly Compton-thick. Fig. 11 shows how dramatic this effect is. Indeed, if the source has $\log N_H \approx 24$ then only ∼50 % of the intrinsic, nuclear, flux is visible above 15 keV. This fraction becomes much lower (e.g. a few %) if the source has $\log N_H \approx 25$. Thus the extreme low number of Compton-thick AGN detected in shallow surveys at hard X-rays is due to fact that only the population of *intrinsically* bright objects is being sampled. As such these objects are rare. For the first time, we use the knowledge of how X-rays are absorbed through a Compton-thick medium to determine the *intrinsic* absorption distribution. We find that Compton-thick AGN are 20^{+9}_{-6} % (statistical error) of the whole AGN population. Our result shows beyond doubt that Compton-thick sources are indeed *intrinsically* numerous, but due to the large absorption, very difficult to detect.

The average spectrum of all Compton-thick AGN detected by BAT is, in the 15-195 keV band, compatible with a very curved spectrum peaking around 40–50 keV (see Fig. 4). Since the peak of the CXB is located at ∼ 25 keV (Ajello et al. 2008b), this implies that the bulk of the Compton-thick AGN must be located at $z \approx 1$ in order to explain the missing fraction of the CXB. We employed the MYTorus model, that fully treats photoelectric absorption and relativistic Compton-scattering in a toroidal geometry, to fit the BAT spectra of the Compton-thick AGN. We derived that in the BAT band the spectrum of Compton-thick AGN is very likely dominated by the scattered component. The photon index is compatible with 2.0 while the absorbing column density is constrained to be Compton-thick using BAT data alone. We also found out that on average only ∼30 % of the intrinsic nuclear flux is visible in the BAT band. A more detailed an analysis on each of the Compton-thick AGN detected by BAT will be reported in a future publication.

Summarizing we find that Compton-thick AGN: 1) are *intrinsically* as numerous as required by the AGN unified model , and 2) have a spectral shape which 'fits' the one required to explain the shape and the peak of the CXB. However, the predictions of population synthesis models (Gilli et al. 2007; Treister et al. 2009) in terms of *observed* Compton-thick

AGN are between a factor of 2 to 3 larger than what is currently observed by BAT.

7.2. A receding torus or a Clumpy torus model ?

It is generally accepted that all kinds of AGN are different manifestations of the same engine (i.e. the accreting super-massive black hole), seen under different line of sights. Thus, in the unified picture, obscuration depends solely on orientation effects. This hypothesis breaks down when showing that the fraction of obscured sources (relative to the whole population) decreases with luminosity. This result has been reported several times in the past, but it has been confirmed now by BAT (with a sample a factor $\sim$2 greater than the one presented in Tueller et al. (2008)).

Our results, like the previous claims of this anti-correlation, are inconsistent with the simplest prediction of the unified model, for which $F_{\%}$ should not depend on L_X. Already Lawrence (1991) tried to overcome this contradiction by proposing a *receding torus model*. In this model, the inner radius is set by the dust sublimation radius which increases with source luminosity. This model predicts that the fraction of obscured sources scales with luminosity as $F_{\%} \propto L^{-0.5}$.

In basic terms (see Nenkova et al. 2008, for a detailed discussion), the inner radius is set from the following:

$$R_d \simeq 0.4 \left(\frac{L}{10^{45} \mathrm{erg\ s^{-1}}} \right)^{0.5} \left(\frac{1500\ \mathrm{K}}{T_{sub}} \right)^{2.6} \mathrm{pc} \quad (10)$$

where L is the bolometric luminosity and T_{sub} is the sublimation temperature of the dust. Given the angular dependence of $F_{\%}$ (i.e. the angle at which a smooth torus becomes transparent to radiation), a constant H/R implies $F_{\%} \propto L^{-0.5}$. While attractive, this simple idea fails to reproduce correctly the dependence of the obscured fraction with luminosity, in particular when looking just at the hard X-ray portion of the spectral energy distribution. Indeed, in this work we showed that $F_{\%} \propto L_X^{-0.26 \pm 0.05}$ for $L_X \geq 10^{42}$ erg s^{-1}.

Nonetheless, one has to consider that (i) the torus is likely clumpy, (ii) H/R is a function of luminosity (Simpson 2005), and (iii) that even if the dusty components of the torus do absorb optical, UV, and X-ray photons, X-ray obscuration can take place also in the -dust free- inner region, in the proximity (< 0.1pc) of the AGN. This has been largely discussed in Risaliti et al. (2002, 2007). Recently (see Hönig & Beckert 2007; Nenkova et al. 2008) $F_{\%}$ was interpreted in the framework of a *radiation-limited clumpy dust torus* in which $F_{\%} \propto L^{-0.25}$, which is much closer to our findings. In this scenario, the obscuration–luminosity relation is recovered in terms of probability that the photons intercept a sufficient number of

clouds in the line of sight. In addition, the work of Hasinger (2008) shows similar results in the 2–10 keV energy band, even if just proxies of N_H are used. Finally, Maiolino et al. (2007) interpreted those early results by comparing them to a similar relation between the fraction of obscured AGN and the O[III] luminosity (as well as other bands, but see their detailed description). According to the authors this was a signature of the variation of the covering factor of the AGN dust with luminosity. The variation of the covering factor of the torus is -in general- also associated with the "Iwasawa-Taniguchi" (IT) effect (Iwasawa & Taniguchi 1993), i.e. the anti-correlation of the EW of FeKα and X-ray luminosity. Bianchi et al. (2009a) discussed the agreement among the findings of Dadina (2008) in the 20-100 keV regime, and their updated *XMM–Newton* sample. If the anti-correlation of $F_{\%}$ and luminosity is interpreted as the variation of the covering factor of the torus, then this can be in turn compared to the IT effect. From the results of Della Ceca et al. (2008), they found a slope of $\simeq 0.22$, in very good agreement with the IT effect, with the slope ($\simeq 0.18$) presented in Maiolino et al. (2007), and eventually with our findings ($\simeq 0.26$). Although these similarities are intriguing, they certainly deserve a profound investigation (which is beyond the goals of this paper). This is even more compelling when considering that the methods differ and in principle sample different materials.

In the low luminosity regime (i.e. below 10^{42} erg s^{-1}), the behavior of the torus is likely more complex than what reported above. Different authors (e.g. Elitzur & Shlosman 2006; Elitzur & Ho 2009) showed that below a bolometric luminosity of $\sim 10^{42}$ erg s^{-1} the torus obscuration region disappears. This results under the assumption that the clouds are generated by a disk-wind outflow, rather then accreted from the galaxy (Krolik & Begelman 1988). In the framework proposed by Elitzur & Shlosman (2006) and Elitzur & Ho (2009) the cloud mass outflow $\dot{M}_{cl}$ is proportional to the mass accretion rate, which is related to the bolometric luminosity via $\dot{M}_{acc} = 0.02 L_{45}/\eta M_{\odot}$ yr^{-1}, η being the accretion efficiency. The ratio $\dot{M}_{cl}/\dot{M}_{acc}$ increases at progressively lower luminosities but since it cannot exceed unity, there is a limiting luminosity at which the system cannot sustain the cloud outflow any longer.

At low luminosities we then expect absorption of X-rays to be less effective, due to the lack of obscuration in the torus. We should then observe a decrease in the fraction of obscured AGN at low luminosity. For the first time, and thanks to BAT, we are able to inspect the behavior of $F_{\%}$ at low luminosities. Indeed, Fig. 16 shows[4] that the fraction of obscured AGN decreases at low luminosities as one would expect if the torus obscuring region would cease to exist. There are no other evidences (perhaps beside this one, but

[4]We caution the reader that within 3σ the behavior of $F_{\%}$ at low luminosity is still compatible with a constant value of 0.8.

see van der Wolk et al. 2010) which shows that the torus disappears at low luminosities, but there are ample evidences that at least the broad line region (BLR) disappears at low luminosities. This happens for two known class of objects: 1) BL Lac sources and 2) low-luminosity type-2 AGN.

BL Lacs are a class of (low-luminosity) blazars characterized by the absence of emission lines in their optical spectrum. Their broad-band spectrum is normally well understood in terms of the Synchrotron-Self Compton model (Maraschi et al. 1992) where the electrons responsible for the synchrotron emission are up-scattering (via inverse Compton) the same synchrotron radiation to high energy. The main difference with the more luminous flat spectrum radio quasars is that in these latter ones an additional high-energy component (refereed to as 'external Compton' component) is normally detected. In the external Compton model photons from the BLR and/or the disk are up-scattered to high energy by the electrons in the jet. It is believed that the absence of lines and of this external components is caused, in BL Lac objects, by the lack of the BLR, and a lower radiation field density. Moreover, BL Lacs are characterized by low Eddington ratios (e.g. $\lambda_{Edd} \simeq 0.01$). Around this Eddington ratio, the accretion process experiences a transition from an optically thick, geometrically thin disk ($\lambda_{Edd} > 0.01$) to a radiatively inefficient geometrically thick disk (Ghisellini et al. 2009). Therefore in blazars with low Eddington ratios, the electrons in the jet find a medium starved of external radiation, weak or no lines are produced, and the AGN is classified as BL Lac.

Another evidence for the absence of BLR at low luminosities is produced by low-luminosity type-2 AGN. These AGN, are sometimes referred to as 'true' type-2 AGN because when observed in polarized light they do not show broad lines (Ho 2008) and hence lack a BLR. How the "local" changes in the accretion regime affect the environment at the BLR and the torus region is non-trivial and debated (according to Nicastro (2000) and Nicastro et al. (2003), the main driver for the disappearance of the BLR appears to be the accretion rate), nonetheless in this framework we find a convincing interpretation of our findings. The clumpy torus, and the BLR progressively disappear, resulting in a less efficient X-ray obscuration. Therefore we should expect $F_{\%}$ to flatten or even to invert its dependence on the luminosity at progressively low Eddington ratios. With future X-ray missions like *NuSTAR* (Harrison et al. 2005), and *NHXM* (Pareschi et al. 2009) it will be possible to sample with better statistics the population of the low-luminosity AGN and to investigate the behavior of the BLR and the torus in greater detail.

8. Summary and conclusion

We addressed the study of a complete, flux limited, sample of local AGN collected by the *Swift*–BAT instrument in the first three years of survey. The sources are listed in Tab. 5, along with their properties. The aim of this work is to characterize the AGN population from two fundamental observables such as the hard X-ray (15–55 keV) luminosity and absorption. To this aim we jointly fitted the BAT spectra with the available follow up in the 0.3–10 keV domain. In the following we briefly review the main findings. We remind the reader that AGN are defined 'absorbed' if the column density for photoelectric absorption exceeds 10^{22} atoms cm^{-2}.

- Performing a stacked analysis of the complete 199 AGN sample, a simple power law model was shown not to account for the continuum emission. In addition we performed the stacked analysis of the different subsamples of sources: unabsorbed, absorbed, and -for the first time- Compton-thick one. The average spectrum of CT sources was found to be dominated (in the BAT band) by the scattered component and its photon index was found to be compatible with ∼2.0. According to our results, only ∼30 % of the source intrinsic flux is visible in the 15–55 keV band.

- We showed that absorbed AGN are characterized by slightly harder spectra (1.91) with respect to the unabsorbed ones (2.00). Nonetheless the distributions are quite broad, resulting in a Kolmogorov-Smirnov probability of 3.5×10^{-3} of belonging to the same parent population.

- We computed the observed N_H distribution, which shows that the observed fraction absorbed sources is 54±4%, with columns peaking at 10^{23} cm^{-2}. The observed fraction of Compton-thick objects is $4.6^{+2.1}_{-1.5}$%, a factor 2 to 3 lower than what predicted from population synthesis models at the fluxes of the BAT survey.

- We estimated the bias of the BAT instrument against the detection of the Compton-thick AGN. We consequently derived the *intrinsic* N_H distribution by integrating the logN-logS in bins of logN_H setting the minimum observed flux of integration so that the limiting intrinsic flux was the same for all the bins. Therefore we showed that even if the CT objects are only a minor fraction of the observed sample, their contribution rises to 20^{+9}_{-6} % in the intrinsic AGN population.

- The relation between the observed fraction of obscured AGN and the hard X-ray luminosity ($F_{\%}$), was found to have different behaviors according to the luminosity regime considered. For luminosities greater then 10^{42} erg s^{-1} we found a monotonic decline with a slope of -0.26±0.05. At smaller luminosities, albeit affected by poor statistics,

we found a flattening of $F_{\%}$ which we interpreted as the manifest disappearance of the obscuring region. In a disk–cloud outflow scenario, this is indeed expected to happen under a critical luminosity, which is of the same order of the luminosity at which we observe the flattening.

- We showed that the obscuration–luminosity relation can be explained by the different X-ray Luminosity Functions of the obscured and unobscured subsamples. This in turn means that absorbed AGN are intrinsically less luminous. This result, if the mass distribution is narrow, points towards a trend in the Eddington ratios in which objects accreting at lower values (thus having smaller effects on their environments) are more absorbed. Obscuring clouds would be able to come closer to the nuclear region without being affected, and bury the AGN.

A key test to improve our findings will be the calculation of the BH masses for the sample. By means of the two physical quantities (i.e. λ_{Edd} and mass) we plan to test whether it is possible to find a sequence relating absorption, Eddington ratio, and mass of the black hole. Some information can already be found in Middleton et al. (2008) and Beckmann et al. (2009). They found that for two different samples of AGN selected in the local Universe, the mean Eddington ratio is in the 0.01-0.06 range. Cappelluti et al. (2010) also showed that, on average, the BAT AGN used in this work have an Eddington ratio of 0.01. Moreover, Middleton et al. (2008) and Beckmann et al. (2009) found that on average unobscured AGN have larger Eddington ratios with respect to obscured ones. This would be consistent with the presence of a trend in λ_{Edd} for non-jetted AGN. The obscured objects could be accreting at lower Eddington ratios and with flatter spectra; the unobscured ones, with steeper spectra, could be accreting slightly more efficiently. By means of this analysis it would be also possible to relate our findings to a physical consistent picture, in the framework of merger driven AGN activity. Indeed, merging of gas-rich galaxies provides an efficient way to funnel large amount of gas and dust to the central black hole and triggers AGN activity (e.g. Kauffmann & Haehnelt 2000; Wyithe & Loeb 2003; Croton et al. 2006). Noteworthy a very recent work by Koss et al. (2010) determined that a considerable fraction (i.e. $\sim$24 %) of the hosts of the BAT AGN have a close companion within 30 kpc and are experiencing a major merging event. This fraction is extremely relevant when compared to a control sample of local (i.e. $z < 0.1$) optically selected narrow-line AGN, where the fraction of interacting companions is $\sim$ 1 %. We counted how many objects of the sample of merging AGN of Koss et al. (2010) are obscured. We found that $\geq$63 % are obscured AGN[5] with an average column density of $\log N_{\rm H} \approx 23.4$. A limitation to this simple picture is that in case of a

[5] For comparison, we remind that in our sample the fraction of obscured sources is $\sim$50 %.

merging event and of a large gas quantity being funneled towards the center, the black hole is expected to accrete with high Eddington ratios (e.g. Di Matteo et al. 2005; Hopkins et al. 2006). According to Fabian (1999) a SMBH accreting at Eddington luminosities should clear the environment from any Compton-thin (e.g. $\log N_H < 24$) column density and therefore transit to a less obscured phase. If the very first phase of the gas-rich merger event is the creation of a Compton-thick AGN, then we would expect it to display large Eddington ratios. However, two of the most famous Compton-thick AGN (Circinus and NGC 4945) display an Eddington ratio far from unity (i.e. $\leq 10^{-2}$, see Gültekin et al. 2009), proving that this argument still escapes a conclusive explanation. The largest hard X-ray selected samples of AGN in the local Universe may shed some light on the physical interpretation of the feedback of black holes on their surroundings.

We are in debt to Tahir Yaqoob and Kendrah Murphy for allowing us to use the results of their model for the transmission of radiation through a Compton-thick medium before publication. We also acknoweldge helpful comments from the referee. The authors acknowledge the use of NED, SIMBAD, and HEASARC. We thank the *Swift* team for the rapid approval of ToO observations. D.B. is in debt to G. Ghisellini and G. Ghirlanda for endless discussions, acknowledges S. Sazonov for stimulating discussions on the dusty torus and the luminosity function, and M. Bolzonella for help with the Binomial statistics computation of errors. D.B. also acknowledges R. Gilli, E. Treister, and P. Severgnini for their kind replies. D.B. is supported through DLR 50 OR 0405. A.C. acknowledges support from the following: ASI-INAF I/23/05 and ASI-INAF I/088/06/0.

Facilities: Swift/BAT, Swift/XRT, XMM/Newton.

REFERENCES

Ajello, M. 2009, arXiv:0902.3033

Ajello, M., Greiner, J., Kanbach, G., Rau, A., Strong, A. W., & Kennea, J. A. 2008a, ApJ, 678, 102

Ajello, M., et al. 2008b, ApJ, 689, 666

—. 2008c, ApJ, 673, 96

—. 2009a, ApJ, 690, 367

—. 2009b, ApJ, 699, 603

Akylas, A., Georgantopoulos, I., Georgakakis, A., Kitsionas, S., & Hatziminaoglou, E. 2006, A&A, 459, 693

Antonucci, R. 1993, ARA&A, 31, 473

Arnaud, K. A. 1996, in Astronomical Society of the Pacific Conference Series, Vol. 101, Astronomical Data Analysis Software and Systems V, ed. G. H. Jacoby & J. Barnes, 17–+

Avni, Y. 1976, ApJ, 210, 642

Barthelmy, S. D., et al. 2005, Space Science Reviews, 120, 143

Beckmann, V., et al. 2009, A&A, 505, 417

Bianchi, S., Bonilla, N. F., Guainazzi, M., Matt, G., & Ponti, G. 2009a, A&A, 501, 915

Bianchi, S., Piconcelli, E., Chiaberge, M., Bailón, E. J., Matt, G., & Fiore, F. 2009b, ApJ, 695, 781

Brandt, W. N., & Hasinger, G. 2005, ARA&A, 43, 827

Brusa, M., et al. 2010, ApJ, 716, 348

Cappelluti, N., Ajello, M., Burlon, D., Krumpe, M., Miyaji, T., Bonoli, S., & Greiner, J. 2010, ApJ, 716, L209

Cappelluti, N., et al. 2007, ApJS, 172, 341

Cappi, M., et al. 2006, A&A, 446, 459

Comastri, A. 2004, in Astrophysics and Space Science Library, Vol. 308, Supermassive Black Holes in the Distant Universe, ed. A. J. Barger, 245–+

Comastri, A., Iwasawa, K., Gilli, R., Vignali, C., & Ranalli, P. 2009, ArXiv: 0910.1025

Comastri, A., Iwasawa, K., Gilli, R., Vignali, C., Ranalli, P., Matt, G., & Fiore, F. 2010, ApJ, 717, 787

Croton, D. J., et al. 2006, MNRAS, 365, 11

Cusumano, G., et al. 2010, ArXiv: 1009.0522

Dadina, M. 2008, A&A, 485, 417

Dai, X., Chartas, G., Eracleous, M., & Garmire, G. P. 2004, ApJ, 605, 45

Della Ceca, R., et al. 2008, A&A, 487, 119

Di Matteo, T., Springel, V., & Hernquist, L. 2005, Nature, 433, 604

Dwelly, T., & Page, M. J. 2006, MNRAS, 372, 1755

Elitzur, M., & Ho, L. C. 2009, ApJ, 701, L91

Elitzur, M., & Shlosman, I. 2006, ApJ, 648, L101

Fabian, A. C. 1999, MNRAS, 308, L39

Gehrels, N. 1986, ApJ, 303, 336

Gehrels, N., et al. 2004, ApJ, 611, 1005

Georgantopoulos, I., Georgakakis, A., & Koulouridis, E. 2005, MNRAS, 360, 782

Ghisellini, G., Haardt, F., & Matt, G. 1994, MNRAS, 267, 743

Ghisellini, G., Maraschi, L., & Tavecchio, F. 2009, MNRAS, 396, L105

Ghisellini, G., et al. 2010, MNRAS, 405, 387

Gilli, R., Comastri, A., & Hasinger, G. 2007, A&A, 463, 79

Gültekin, K., Cackett, E. M., Miller, J. M., Di Matteo, T., Markoff, S., & Richstone, D. O. 2009, ApJ, 706, 404

Harrison, F. A., et al. 2005, Experimental Astronomy, 20, 131

Hasinger, G. 2008, A&A, 490, 905

Hasinger, G., Miyaji, T., & Schmidt, M. 2005, A&A, 441, 417

Ho, L. C. 2008, ARA&A, 46, 475

Hogg, D. W. 1999, ArXiv:astro-ph/9905116

Hönig, S. F., & Beckert, T. 2007, MNRAS, 380, 1172

Hopkins, P. F., Hernquist, L., Cox, T. J., Di Matteo, T., Robertson, B., & Springel, V. 2006, ApJS, 163, 1

Hopkins, P. F., Hickox, R., Quataert, E., & Hernquist, L. 2009, MNRAS, 398, 333

Ishibashi, W., & Courvoisier, T. 2010, A&A, 512, A58+

Iwasawa, K., Fabian, A. C., & Matt, G. 1997, MNRAS, 289, 443

Iwasawa, K., & Taniguchi, Y. 1993, ApJ, 413, L15

Jiménez-Bailón, E., Santos-Lleó, M., Piconcelli, E., Matt, G., Guainazzi, M., & Rodríguez-Pascual, P. 2007, A&A, 461, 917

Kalberla, P. M. W., Burton, W. B., Hartmann, D., Arnal, E. M., Bajaja, E., Morras, R., & Pöppel, W. G. L. 2005, A&A, 440, 775

Kauffmann, G., & Haehnelt, M. 2000, MNRAS, 311, 576

Koss, M., Mushotzky, R., Veilleux, S., & Winter, L. 2010, ApJ, 716, L125

Krolik, J. H., & Begelman, M. C. 1988, ApJ, 329, 702

La Franca, F., et al. 2005, ApJ, 635, 864

Lawrence, A. 1991, MNRAS, 252, 586

Lawrence, A., & Elvis, M. 1982, ApJ, 256, 410

Maiolino, R., Shemmer, O., Imanishi, M., Netzer, H., Oliva, E., Lutz, D., & Sturm, E. 2007, A&A, 468, 979

Malizia, A., Stephen, J. B., Bassani, L., Bird, A. J., Panessa, F., & Ubertini, P. 2009, MNRAS, 399, 944

Maraschi, L., Ghisellini, G., & Celotti, A. 1992, ApJ, 397, L5

Markwardt, C. B., Tueller, J., Skinner, G. K., Gehrels, N., Barthelmy, S. D., & Mushotzky, R. F. 2005, ApJ, 633, L77

Matt, G., Bianchi, S., Awaki, H., Comastri, A., Guainazzi, M., Iwasawa, K., Jimenez-Bailon, E., & Nicastro, F. 2009, A&A, 496, 653

Matt, G., Bianchi, S., Guainazzi, M., & Molendi, S. 2004, A&A, 414, 155

Matt, G., Pompilio, F., & La Franca, F. 1999, New Astronomy, 4, 191

Middleton, M., Done, C., & Schurch, N. 2008, MNRAS, 383, 1501

Murphy, K. D., & Yaqoob, T. 2009, MNRAS, 397, 1549

Nandra, K., & Pounds, K. A. 1994, MNRAS, 268, 405

Nenkova, M., Sirocky, M. M., Nikutta, R., Ivezić, Ž., & Elitzur, M. 2008, ApJ, 685, 160

Nicastro, F. 2000, ApJ, 530, L65

Nicastro, F., Martocchia, A., & Matt, G. 2003, ApJ, 589, L13

Norman, C., et al. 2004, ApJ, 607, 721

Page, K. L., Reeves, J. N., O'Brien, P. T., & Turner, M. J. L. 2005, MNRAS, 364, 195

Paltani, S., Walter, R., McHardy, I. M., Dwelly, T., Steiner, C., & Courvoisier, T. J.-L. 2008, A&A, 485, 707

Pareschi, G., et al. 2009, in Society of Photo-Optical Instrumentation Engineers (SPIE) Conference Series, Vol. 7437, Society of Photo-Optical Instrumentation Engineers (SPIE) Conference Series

Parisi, P., et al. 2009, A&A, 507, 1345

Piconcelli, E., Bianchi, S., Guainazzi, M., Fiore, F., & Chiaberge, M. 2007, A&A, 466, 855

Ranalli, P., Comastri, A., & Setti, G. 2003, A&A, 399, 39

Reeves, J. N., & Turner, M. J. L. 2000, MNRAS, 316, 234

Risaliti, G., Elvis, M., Fabbiano, G., Baldi, A., Zezas, A., & Salvati, M. 2007, ApJ, 659, L111

Risaliti, G., Elvis, M., & Nicastro, F. 2002, ApJ, 571, 234

Risaliti, G., Maiolino, R., & Salvati, M. 1999, ApJ, 522, 157

Risaliti, G., et al. 2009, MNRAS, 393, L1

Saez, C., Chartas, G., Brandt, W. N., Lehmer, B. D., Bauer, F. E., Dai, X., & Garmire, G. P. 2008, AJ, 135, 1505

Sazonov, S., Revnivtsev, M., Krivonos, R., Churazov, E., & Sunyaev, R. 2007, A&A, 462, 57

Sazonov, S. Y., & Revnivtsev, M. G. 2004, A&A, 423, 469

Severgnini, P., Caccianiga, A., Della Ceca, R., Braito, V., Vignali, C., La Parola, V., & Moretti, A. 2010, ArXiv: 1010.2085

Shinozaki, K., Miyaji, T., Ishisaki, Y., Ueda, Y., & Ogasaka, Y. 2006, AJ, 131, 2843

Shu, X. W., Wang, J. X., Jiang, P., Fan, L. L., & Wang, T. G. 2007, ApJ, 657, 167

Simpson, C. 2005, MNRAS, 360, 565

Treister, E., & Urry, C. M. 2006, ApJ, 652, L79

Treister, E., Urry, C. M., & Virani, S. 2009, ApJ, 696, 110

Tueller, J., Mushotzky, R. F., Barthelmy, S., Cannizzo, J. K., Gehrels, N., Markwardt, C. B., Skinner, G. K., & Winter, L. M. 2008, ApJ, 681, 113

Tueller, J., et al. 2010, ApJS, 186, 378

Ueda, Y., Akiyama, M., Ohta, K., & Miyaji, T. 2003, ApJ, 598, 886

Ueda, Y., et al. 2007, ApJ, 664, L79

Urry, C. M., & Padovani, P. 1995, PASP, 107, 803

van der Wolk, G., Barthel, P. D., Peletier, R. F., & Pel, J. W. 2010, A&A, 511, A64+

Voss, R., & Ajello, M. 2010, ApJ, 721, 1843

Winter, L. M., Mushotzky, R. F., Reynolds, C. S., & Tueller, J. 2009a, ApJ, 690, 1322

Winter, L. M., Mushotzky, R. F., Terashima, Y., & Ueda, Y. 2009b, ApJ, 701, 1644

Winter, L. M., Mushotzky, R. F., Tueller, J., & Markwardt, C. 2008, ApJ, 674, 686

Worsley, M. A., et al. 2005, MNRAS, 357, 1281

Wyithe, J. S. B., & Loeb, A. 2003, ApJ, 595, 614

Yaqoob, T. 1997, ApJ, 479, 184

Yaqoob, T., Murphy, K. D., Miller, L., & Turner, T. J. 2010, MNRAS, 401, 411

Table 5. *Swift* sample of AGN.

SWIFT NAME	R.A. (J2000)	DEC (J2000)	Flux [15-55 keV] (10^{-11} cgs)	S/N	ID	Type‡	redshift	Ph. Index (BAT only)	log(N_H)	Reference
J0006.4+2009	1.600	20.152	1.16±0.20	5.8	Mrk 335	Sy1	0.03	$2.38^{+0.50}_{-0.42}$	22.6	(2)
J0038.6+2336	9.650	23.600	1.10±0.21	5.3	Mrk 344	Sy	0.02	$2.06^{+0.46}_{-0.41}$	23.2	(2)
J0042.7-2332	10.680	-23.548	2.44±0.21	11.7	NGC 235A	Sy2	0.02	$1.60^{+0.20}_{-0.19}$	23.0	(1)
J0048.7+3157	12.188	31.962	7.71±0.20	37.8	Mrk 348	Sy2	0.02	$1.90^{+0.08}_{-0.07}$	23.3	(1)
J0051.9+1726	12.998	17.447	1.81±0.21	8.6	QSO B0049+171	Sy1	0.06	$2.13^{+0.28}_{-0.25}$	20.0	(2)
J0059.9+3149	14.997	31.831	1.66±0.21	8.0	SWIFT J0059.4+3150	Sy1.2	0.01	$1.93^{+0.35}_{-0.32}$	21.0	(1)
J0101.0-4748	15.274	-47.800	0.97±0.18	5.6	2MASX J01003469-4748303	GALAXY	0.08	$2.32^{+0.44}_{-0.38}$	22.6	(2)
J0108.8+1321	17.201	13.351	1.78±0.22	8.2	4C 13.07	Sy2	0.06	$1.76^{+0.34}_{-0.27}$	23.8	(3)
J0111.4-3805	17.867	-38.086	1.52±0.18	8.3	**NGC 424**	Sy2	0.01	$1.94^{+0.28}_{-0.27}$	24.3	(4)
J0113.8-1450	18.453	-14.850	1.24±0.21	5.8	Mrk 1152	Sy1	0.05	$2.10^{+0.38}_{-0.34}$	21.1	(5)
J0114.3-5524	18.600	-55.400	0.92±0.17	5.3	SWIFT J0114.4-5522	Sy2	0.01	$1.53^{+0.33}_{-0.38}$	22.9	(1)
J0123.8-5847	20.952	-58.785	2.65±0.17	15.3	Fairall 9	Sy1	0.05	$2.02^{+0.15}_{-0.15}$	20.4	(1)
J0123.8-3504	20.974	-35.067	2.72±0.18	14.7	NGC 526A	Sy1.5	0.02	$1.71^{+0.14}_{-0.14}$	22.3	(1)
J0127.9-1850	22.000	-18.847	1.27±0.20	6.2	MCG-03-04-072	Sy1	0.04	$2.26^{+0.54}_{-0.44}$	20.0	(2)
J0134.0-3629	23.506	-36.486	2.36±0.18	13.0	NGC 612	Sy2	0.03	$1.63^{+0.17}_{-0.15}$	23.7	(6)
J0138.6-4000	24.674	-40.008	3.17±0.18	18.0	ESO 297-018	Sy2	0.03	$1.71^{+0.11}_{-0.11}$	23.8	(7)
J0142.6+0118	25.652	1.300	1.28±0.22	5.7	[VV2003c] J014214.0+011615	Sy1	0.05	$2.52^{+1.10}_{-0.57}$	...	
J0152.9-0326	28.250	-3.448	1.47±0.22	6.6	IGR J01528-0326	Sy2	0.02	$2.28^{+0.48}_{-0.41}$	22.9	(2)
J0201.2-0649	30.320	-6.821	4.17±0.22	19.3	NGC 788	Sy2	0.01	$1.74^{+0.11}_{-0.11}$	23.5	(1)
J0206.5-0016	31.631	-0.270	1.53±0.22	6.9	MRK 1018	Sy1.5	0.04	$1.48^{+0.40}_{-0.39}$	20.5	(1)
J0215.0-0044	33.751	-0.749	1.30±0.22	5.9	Mrk 590	Sy1.2	0.03	$2.23^{+0.54}_{-0.47}$	20.4	(1)
J0226.0-6315	36.500	-63.250	0.91±0.18	5.2	FAIRALL 0926	Sy1	0.06	$2.55^{+0.57}_{-0.47}$	20.9	(2)
J0226.8-2819	36.703	-28.324	1.14±0.18	6.4	2MASX J02262568-2820588	Sy1	0.06	$2.21^{+0.59}_{-0.49}$	21.8	(2)
J0228.4+3118	37.120	31.316	4.38±0.23	19.4	NGC 931	Sy1.5	0.02	$2.25^{+0.22}_{-0.16}$	21.6	(1)
J0232.0-3639	38.020	-36.662	1.09±0.17	6.4	IC 1816	Sy2	0.02	$2.03^{+0.38}_{-0.34}$	23.9	(2)
J0234.4+3229	38.612	32.489	1.60±0.23	7.1	NGC 973	Sy2	0.02	$1.70^{+0.41}_{-0.33}$	22.5	(2)
J0234.8-0847	38.702	-8.794	2.13±0.21	10.2	NGC 985	Sy1	0.04	$2.23^{+0.26}_{-0.24}$	21.6	(1)
J0235.6-2935	38.900	-29.600	0.99±0.18	5.6	ESO 0416-G0002	Sy1.9	0.06	$1.62^{+0.45}_{-0.35}$	19.6	(1)
J0238.5-5213	39.647	-52.220	1.31±0.17	7.6	ESO 198-024	Sy1	0.05	$1.69^{+0.26}_{-0.25}$	21.0	(1)
J0239.0-4043	39.767	-40.732	0.97±0.17	5.8	2MASX J02384897-4038377	Sy1	0.06	$2.12^{+0.61}_{-0.52}$	20.0	(2)
J0241.5-0813	40.381	-8.220	1.34±0.21	6.4	NGC 1052	Sy2	0.01	$1.47^{+0.38}_{-0.38}$	20.5	(8)
J0242.9-0000	40.732	-0.012	2.00±0.22	8.9	**NGC 1068**	Sy2	0.004	$2.23^{+0.33}_{-0.30}$	>25	(4)
J0249.3+2627	42.349	26.451	1.25±0.23	5.5	IRAS 02461+2618	Sy2	0.06	$1.66^{+0.39}_{-0.38}$	23.5	(2)
J0252.8-0830	43.200	-8.500	1.06±0.21	5.0	MCG-02-08-014	Sy2	0.02	$1.69^{+0.54}_{-0.40}$	23.1	(2)

Table 5—Continued

SWIFT NAME	R.A. (J2000)	DEC (J2000)	Flux [15-55 keV] (10^{-11} cgs)	S/N	ID	Type‡	redshift	Ph. Index (BAT only)	log(N_H)	Reference
J0255.4-0010	43.873	-0.170	4.48±0.22	20.1	NGC 1142	Sy2	0.03	$1.85^{+0.12}_{-0.11}$	23.4	(9)
J0256.4-3212	44.117	-32.208	1.31±0.17	7.7	ESO 417-6	Sy2	0.02	$1.86^{+0.25}_{-0.24}$	22.9	(2)
J0311.6-2045	47.919	-20.760	1.27±0.18	6.9	2MASX J03111883-2046184	Sy1	0.07	$1.79^{+0.43}_{-0.34}$	20.0	(2)
J0325.1+3409	51.296	34.152	1.61±0.24	6.8	2MASX J03244119+3410459	Sy1	0.06	$1.56^{+0.42}_{-0.30}$	20.0	(2)
J0333.5+3716	53.397	37.278	1.63±0.24	6.8	IGR J03334+3718	Sy1	0.06	$2.37^{+0.53}_{-0.44}$	20.0	(2)
J0333.7-3608	53.433	-36.141	3.12±0.17	18.9	NGC 1365	Sy1.8	0.01	$2.02^{+0.25}_{-0.24}$	23.6	(1)
J0342.2-2114	55.554	-21.244	2.15±0.18	11.8	SWIFT J0342.0-2115	Sy1	0.01	$1.88^{+0.20}_{-0.19}$	20.5	(1)
J0347.3-3029	56.850	-30.500	0.89±0.17	5.3	RBS 0741	Sy1	0.10	$2.04^{+0.48}_{-0.43}$	20.4	(2)
J0350.7-5022	57.679	-50.377	1.29±0.17	7.5	SWIFT J0350.1-5019	Sy2	0.04	$1.79^{+0.39}_{-0.29}$	23.2	(2)
J0357.0-4039	59.268	-40.666	0.89±0.17	5.4	2MASX J03565655-4041453	Sy1.9	0.07	$1.56^{+0.35}_{-0.34}$	22.5	(1)
J0402.5-1804	60.639	-18.077	1.35±0.19	7.0	ESO 549- G049	Sy2	0.03	$1.75^{+0.50}_{-0.38}$	22.4	(2)
J0407.5+0342	61.883	3.717	1.90±0.25	7.6	3C 105	Sy2	0.09	$1.91^{+0.30}_{-0.28}$	23.4	(1)
J0415.2-0753	63.800	-7.900	1.31±0.23	5.6	LEDA 14727	Sy1	0.04	$2.25^{+0.44}_{-0.39}$	23.5	(2)
J0426.4-5712	66.603	-57.201	1.40±0.17	8.2	1H 0419-577	Sy1	0.10	$2.57^{+0.56}_{-0.33}$	19.5	(1)
J0433.4+0521	68.355	5.365	5.21±0.26	19.8	3C-120	Sy1	0.03	$2.12^{+0.13}_{-0.12}$	21.2	(1)
J0438.5-1049	69.633	-10.830	1.48±0.23	6.4	MCG-02-12-050	Sy1	0.04	$2.02^{+0.61}_{-0.53}$	20.0	(2)
J0444.7-2812	71.199	-28.200	1.07±0.18	5.9	2MASX J04450628-2820284	Sy2	0.15	$2.17^{+0.88}_{-0.66}$	20.0	(2)
J0451.8-5807	72.966	-58.133	0.88±0.17	5.2	RBS 0594	Sy1	0.09	$1.86^{+0.42}_{-0.38}$	20.0	(2)
J0453.5+0403	73.380	4.060	2.11±0.28	7.6	**CGCG 420-015**	Sy2	0.03	$2.04^{+0.36}_{-0.33}$	∼24.2	(4)
J0455.3-7528	73.841	-75.477	1.27±0.18	6.9	ESO 33-2	Sy2	0.02	$2.52^{+0.49}_{-0.41}$	22.1	(2)
J0505.9-2351	76.497	-23.854	2.78±0.20	13.9	XSS J05054-2348	Sy2	0.04	$1.79^{+0.18}_{-0.17}$	22.7	(1)
J0516.2-0009	79.071	-0.161	4.11±0.28	14.5	QSO B0513-002	Sy1	0.03	$2.16^{+0.17}_{-0.16}$	20.0	(2)
J0519.7-3240	79.930	-32.676	2.38±0.19	12.9	SWIFT J0519.5-3140	Sy2	0.04	$1.72^{+0.18}_{-0.14}$	21.1	(1)
J0519.8-4546	79.963	-45.774	2.49±0.17	14.9	Pictor-A	Sy1	0.04	$1.90^{+0.17}_{-0.17}$	21.0	(1)
J0524.2-1212	81.050	-12.200	1.42±0.25	5.6	LEDA 17233	Sy1	0.05	$1.90^{+0.36}_{-0.33}$	21.2	(2)
J0552.3-0727	88.090	-7.457	14.75±0.29	51.7	NGC 2110	Sy2	0.01	$1.79^{+0.00}_{-0.00}$	22.6	(1)
J0552.3+5929	88.100	59.500	1.14±0.21	5.3	IRAS 05480+5927	Sy1	0.06	$3.44^{+1.00}_{-0.73}$	21.1	(2)
J0558.1-3820	89.549	-38.347	2.12±0.18	11.6	EXO 055620-3820.2	Sy1	0.03	$2.21^{+0.23}_{-0.21}$	22.2	(1)
J0602.9-8633	90.749	-86.555	1.82±0.22	8.4	**SWIFT J0601.9-8636**	Sy2	0.01	$1.67^{+0.24}_{-0.37}$	∼24	(4)
J0603.1+6523	90.799	65.399	1.38±0.20	6.8	UGC 3386	GALAXY	0.02	$2.10^{+0.36}_{-0.33}$	23.2	(3)
J0615.8+7101	93.967	71.021	6.08±0.20	30.8	Mrk 3	Sy2	0.01	$1.66^{+0.01}_{-0.01}$	24.0	(1)
J0623.9-3214	95.994	-32.248	1.53±0.20	7.5	ESO 426-G 002	Sy2	0.02	$1.86^{+0.38}_{-0.35}$	23.9	(2)
J0624.1-6059	96.028	-60.998	1.25±0.17	7.4	SWIFT J2141.0+1603	Sy2	0.04	$2.51^{+0.42}_{-0.36}$	23.4	(2)
J0640.7-4324	100.200	-43.400	0.92±0.18	5.2	2MASX J06400609-4327591	Sy2	0.06	$2.06^{+0.44}_{-0.39}$	23.4	(2)

Table 5—Continued

SWIFT NAME	R.A. (J2000)	DEC (J2000)	Flux [15-55 keV] (10^{-11} cgs)	S/N	ID	Type‡	redshift	Ph. Index (BAT only)	log(N_H)	Reference
J0652.1+7425	103.044	74.425	3.29±0.19	17.1	Mrk 6	Sy1.5	0.02	$1.89^{+0.13}_{-0.13}$	23.0	(1)
J0656.1+3959	104.027	39.986	2.29±0.26	8.7	UGC 3601	Sy1	0.02	$1.97^{+0.29}_{-0.27}$	21.3	(2)
J0718.0+4405	109.517	44.084	1.67±0.24	7.1	2MASX J07180060+4405271	Sy1	0.06	$2.22^{+0.41}_{-0.35}$	20.0	(2)
J0742.5+4947	115.644	49.793	2.98±0.21	14.4	Mrk 79	Sy1.2	0.02	$2.06^{+0.17}_{-0.16}$	20.8	(1)
J0800.1+2322	120.032	23.370	1.62±0.24	6.6	SDSS J0759.87+232448.3	GALAXY	0.03	$1.70^{+0.31}_{-0.30}$	22.3	(2)
J0800.3+2638	120.099	26.648	1.79±0.24	7.5	IC 486	Sy1	0.03	$1.80^{+0.30}_{-0.28}$	22.2	(2)
J0804.2+0506	121.050	5.101	3.18±0.25	12.6	UGC 4203	Sy2	0.01	$2.58^{+0.60}_{-0.48}$	23.5	(10)
J0811.1+7602	122.798	76.049	1.15±0.19	6.2	PG 0804+761	Sy1	0.10	$2.58^{+0.60}_{-0.48}$	20.0	(2)
J0814.4+0423	123.600	4.400	1.26±0.24	5.2	CGCG 031-072	Sy1	0.03	$1.90^{+0.49}_{-0.42}$	23.3	(2)
J0823.2-0456	125.800	-4.947	1.35±0.23	6.0	SWIFT J0823.4-0457	Sy2	0.02	$1.66^{+0.38}_{-0.37}$	23.5	(3)
J0832.8+3706	128.200	37.100	1.03±0.20	5.2	RBS 707	Sy1.2	0.09	$2.41^{+0.63}_{-0.52}$	20.0	(2)
J0839.8-1214	129.950	-12.248	1.28±0.21	6.1	3C 206	Sy1	0.20	$2.04^{+0.34}_{-0.31}$	21.0	(2)
J0904.9+5537	136.250	55.632	1.04±0.17	6.0	SWIFT J0904.3+5538	Sy1.5	0.04	$1.92^{+0.42}_{-0.39}$	21.0	(1)
J0911.5+4528	137.898	45.471	1.23±0.18	7.0	SWIFT J0911.2+4533	Sy2	0.03	$2.45^{+0.54}_{-0.44}$	23.5	(1)
J0918.4+1618	139.615	16.316	1.65±0.21	8.0	Mrk 704	Sy1.5	0.03	$1.98^{+0.26}_{-0.24}$	21.5	(2)
J0921.0-0803	140.257	-8.067	2.59±0.20	12.9	SWIFT J0920.8-0805	Sy2	0.02	$2.15^{+0.21}_{-0.19}$	22.8	(1)
J0923.8+2256	140.962	22.936	2.05±0.20	10.5	MCG +04-22-042	Sy1.2	0.03	$1.85^{+0.23}_{-0.21}$	20.6	(1)
J0925.2+5217	141.316	52.285	3.03±0.17	18.1	Mrk 110	Sy1	0.04	$2.00^{+0.14}_{-0.13}$	20.6	(1)
J0945.8-1419	146.468	-14.332	1.28±0.21	6.1	NGC 2992	Sy2	0.01	$1.55^{+0.34}_{-0.33}$	22.0	(1)
J0947.7-3056	146.939	-30.948	11.50±0.22	51.5	ESO 434-40	Sy2	0.01	$2.27^{+0.01}_{-0.01}$	22.2	(3)
J0959.6-2250	149.916	-22.834	4.44±0.22	19.8	NGC 3081	Sy2	0.01	$1.80^{+0.13}_{-0.12}$	23.5	(1)
J1001.8+5542	150.453	55.700	1.43±0.16	8.8	**NGC 3079**	Sy2	0.004	$1.88^{+0.26}_{-0.25}$	24.7	(4)
J1006.0-2306	151.500	-23.100	1.25±0.23	5.5	ESO 499-G 041	Sy1	0.01	$1.57^{+0.60}_{-0.62}$	21.4	(2)
J1021.7-0327	155.450	-3.450	1.35±0.22	6.3	MCG+00-27-002	Sy1	0.04	$2.34^{+0.54}_{-0.44}$	20.0	(2)
J1023.5+1951	155.888	19.864	7.35±0.20	36.8	NGC 3227	Sy1.5	0.004	$1.98^{+0.01}_{-0.01}$	22.8	(1)
J1031.8-3451	157.975	-34.860	4.71±0.26	18.4	NGC 3281	Sy2	0.01	$1.98^{+0.17}_{-0.16}$	23.9	(6)
J1031.9-1417	157.996	-14.300	2.13±0.23	9.3	H 1029-140	Sy1	0.09	$2.17^{+0.32}_{-0.29}$	20.0	(2)
J1044.0+7023	161.003	70.400	0.99±0.17	5.9	MCG+12-10-067	Sy2	0.03	$1.60^{+0.37}_{-0.35}$	23.3	(2)
J1046.5+2556	161.649	25.950	1.12±0.19	5.9	UGC 05881	GALAXY	0.02	$1.60^{+0.38}_{-0.36}$	23.0	(2)
J1048.5-2512	162.149	-25.200	1.42±0.27	5.3	**NGC 3393**	Sy2	0.01	$2.01^{+0.43}_{-0.37}$	24.7	(4)
J1049.3+2256	162.350	22.950	1.57±0.20	8.0	SWIFT J1049.4+2258	Sy2	0.03	$1.89^{+0.24}_{-0.23}$	23.3	(2)
J1106.6+7234	166.654	72.571	6.45±0.17	38.0	NGC 3516	Sy1.5	0.01	$1.90^{+0.01}_{-0.01}$	21.2	(1)
J1115.9+5426	168.999	54.450	0.88±0.15	5.7	SDSS J111519.98+542316.6	Sy2	0.07	$1.80^{+0.57}_{-0.42}$	22.4	(2)
J1125.4+5421	171.352	54.351	0.97±0.15	6.3	ARP 151	Sy1	0.02	$1.72^{+0.48}_{-0.37}$	20.0	(2)

Table 5—Continued

SWIFT NAME	R.A. (J2000)	DEC (J2000)	Flux [15-55 keV] (10^{-11} cgs)	S/N	ID	Type‡	redshift	Ph. Index (BAT only)	log(N_H)	Reference
J1127.5+1908	171.900	19.148	1.12±0.20	5.6	1RXS J112716.6+190914	Sy1	0.10	$1.84^{+0.62}_{-0.54}$	21.4	(2)
J1132.7+5259	173.188	52.988	1.01±0.15	6.6	UGC 6527	Sy1	0.03	$1.85^{+0.36}_{-0.34}$	20.0	(3)
J1136.5+2132	174.150	21.548	1.13±0.19	5.9	Mrk 739	Sy1	0.03	$3.06^{+0.64}_{-0.53}$	20.7	(2)
J1139.0-3744	174.764	-37.741	10.07±0.27	37.9	NGC 3783	Sy1	0.01	$1.94^{+0.01}_{-0.01}$	22.5	(1)
J1139.1+5912	174.783	59.212	1.25±0.15	8.1	SBS 1136+594	Sy1.5	0.06	$2.76^{+0.46}_{-0.39}$	19.6	(1)
J1139.4+3156	174.869	31.935	1.00±0.17	5.8	NGC 3786	Sy1.8	0.01	$1.74^{+0.45}_{-0.34}$	22.5	(3)
J1144.7+7939	176.190	79.662	2.13±0.18	11.9	SWIFT J1143.7+7942	Sy1.2	0.02	$2.26^{+0.24}_{-0.23}$	20.6	(1)
J1145.3+5859	176.349	59.000	0.81±0.15	5.3	Ark 320	GALAXY	0.01	$2.23^{+0.74}_{-0.55}$	22.2	(2)
J1145.5-1825	176.393	-18.428	2.84±0.27	10.5	2MASX J11454045-1827149	Sy1	0.03	$2.02^{+0.22}_{-0.21}$	20.5	(1)
J1148.9+2938	177.230	29.634	1.06±0.18	6.1	MCG+05-28-032	LINER	0.02	$1.85^{+0.39}_{-0.35}$	22.5	(2)
J1158.0+5526	179.502	55.449	1.04±0.15	6.9	NGC 3998	Sy1	0.003	$2.05^{+0.40}_{-0.41}$	20.1	(8)
J1201.0+0647	180.250	6.800	1.18±0.21	5.6	SWIFT J1200.8+0650	Sy2	0.04	$1.89^{+0.33}_{-0.30}$	22.8	(1)
J1203.0+4432	180.773	44.534	2.33±0.15	15.1	NGC 4051	Sy1.5	0.002	$2.45^{+0.18}_{-0.17}$	20.5	(1)
J1204.5+2018	181.149	20.301	1.32±0.19	7.1	ARK 347	Sy2	0.02	$1.76^{+0.29}_{-0.23}$	23.2	(1)
J1206.2+5242	181.565	52.710	1.24±0.15	8.3	NGC 4102	LINER	0.003	$1.74^{+0.30}_{-0.28}$	20.9	(1)
J1209.1+4700	182.300	47.000	0.76±0.15	5.0	Mrk 198	Sy2	0.02	$1.76^{+0.47}_{-0.36}$	22.8	(2)
J1209.4+4341	182.370	43.686	1.56±0.15	10.1	NGC 4138	Sy1.9	0.003	$1.90^{+0.22}_{-0.21}$	22.9	(1)
J1210.5+3924	182.633	39.406	24.60±0.16	153.4	NGC 4151	Sy1.5	0.003	$1.93^{+0.01}_{-0.01}$	22.5	(1)
J1210.6+3819	182.667	38.333	0.96±0.16	6.0	LEDA 38759	Sy1	0.02	$1.91^{+0.35}_{-0.33}$	22.6	(2)
J1217.2+0711	184.300	7.200	1.21±0.20	5.9	NGC 4235	Sy1	0.01	$1.59^{+0.44}_{-0.44}$	21.2	(3)
J1218.3+2950	184.593	29.839	1.53±0.17	9.1	Mrk 766	Sy1.5	0.01	$3.07^{+0.42}_{-0.36}$	21.7	(1)
J1219.0+4715	184.750	47.252	0.96±0.15	6.3	NGC 4258	Sy1	0.001	$1.92^{+0.37}_{-0.34}$	22.9	(11)
J1222.0+7518	185.503	75.311	1.27±0.17	7.4	Mrk 205	Sy1	0.07	$2.53^{+0.42}_{-0.37}$	20.7	(12)
J1225.7+1239	186.447	12.665	12.58±0.19	65.6	NGC 4388	Sy2	0.01	$1.84^{+0.01}_{-0.01}$	23.6	(1)
J1225.8+3330	186.466	33.513	1.25±0.16	7.7	NGC 4395	Sy1	0.001	$2.15^{+0.27}_{-0.25}$	22.3	(1)
J1235.6-3955	188.902	-39.919	10.21±0.26	39.4	NGC 4507	Sy2	0.01	$1.98^{+0.19}_{-0.14}$	23.5	(1)
J1238.8-2718	189.723	-27.308	4.39±0.28	15.9	ESO 506-027	Sy2	0.02	$1.74^{+0.13}_{-0.13}$	23.6	(9)
J1239.0-1611	189.769	-16.196	2.02±0.26	7.7	XSS J12389-1614	Sy2	0.04	$1.68^{+0.28}_{-0.22}$	22.5	(1)
J1239.5-0520	189.898	-5.341	4.52±0.23	19.8	NGC 4593	Sy1	0.01	$1.91^{+0.11}_{-0.11}$	20.3	(1)
J1246.6+5434	191.661	54.575	1.34±0.15	9.0	NGC 4686	LINER	0.02	$1.75^{+0.25}_{-0.20}$	23.8	(2)
J1302.8+1624	195.700	16.400	0.90±0.17	5.1	Mrk 0783	Sy1.2	0.07	$1.92^{+0.43}_{-0.41}$	21.0	(2)
J1306.7-4024	196.698	-40.415	2.37±0.27	8.9	ESO 323-077	Sy1.2	0.02	$2.03^{+0.27}_{-0.25}$	22.7	(2)
J1309.1+1137	197.279	11.632	2.19±0.18	12.0	SWIFT J1309.2+1139	Sy2	0.03	$1.63^{+0.15}_{-0.15}$	23.4	(13)
J1315.4+4424	198.852	44.404	1.28±0.15	8.4	IGR J13149+4422	Sy	0.04	$2.28^{+0.31}_{-0.28}$	22.8	(2)

Table 5—Continued

SWIFT NAME	R.A. (J2000)	DEC (J2000)	Flux [15-55 keV] (10^{-11} cgs)	S/N	ID	Type‡	redshift	Ph. Index (BAT only)	log(N_H)	Reference
J1322.3-1642	200.591	-16.716	2.57±0.27	9.5	MCG -03-34-064	Sy1.8	0.02	$2.15^{+0.30}_{-0.28}$	23.6	(1)
J1325.4-4301	201.366	-43.017	49.77±0.26	187.6	Cen A	Sy2	0.002	$1.85^{+0.00}_{-0.00}$	22.7	(1)
J1334.8-2323	203.700	-23.400	1.49±0.29	5.1	ESO 509-38	Sy2	0.03	$2.37^{+0.69}_{-0.54}$	20.0	(2)
J1335.7-3418	203.944	-34.302	4.86±0.29	16.6	MCG -06-30-015	Sy1.2	0.01	$2.24^{+0.17}_{-0.17}$	21.7	(1)
J1338.1+0433	204.547	4.552	3.63±0.20	17.9	NGC 5252	Sy2	0.02	$1.67^{+0.12}_{-0.12}$	22.64	(13)
J1341.4+3022	205.356	30.369	1.15±0.16	7.2	Mrk 268	Sy2	0.04	$2.38^{+0.35}_{-0.30}$	23.3	(2)
J1349.5-3018	207.390	-30.304	17.87±0.31	58.2	IC 4329A	Sy1	0.02	$2.05^{+0.00}_{-0.00}$	21.6	(1)
J1353.2+6919	208.305	69.327	2.78±0.17	16.7	Mrk 279	Sy1.5	0.03	$1.96^{+0.15}_{-0.15}$	20.5	(1)
J1356.1+3835	209.033	38.583	1.22±0.16	7.7	Mrk 464	Sy1	0.05	$1.69^{+0.30}_{-0.29}$	20.0	(3)
J1408.4-3024	212.100	-30.400	1.65±0.32	5.1	PGC 050427	Sy1	0.02	$2.67^{+0.65}_{-0.52}$	21.2	(2)
J1413.5-0312	213.375	-3.201	14.38±0.24	59.0	NGC 5506	Sy1.9	0.01	$2.27^{+0.11}_{-0.14}$	22.5	(1)
J1418.2+2507	214.568	25.133	3.12±0.17	18.2	NGC 5548	Sy1.5	0.02	$1.82^{+0.12}_{-0.12}$	20.4	(1)
J1419.5-2639	214.893	-26.663	3.49±0.34	10.4	ESO 511-G030	Sy1	0.02	$2.11^{+0.22}_{-0.20}$	21.2	(1)
J1421.6+4750	215.420	47.838	1.03±0.16	6.4	QSO B1419+480	Sy1	0.07	$1.73^{+0.35}_{-0.27}$	21.3	(3)
J1424.3+2435	216.100	24.600	0.89±0.17	5.1	NGC 5610	GALAXY	0.02	$1.88^{+0.46}_{-0.42}$	22.8	(2)
J1429.6+0117	217.400	1.300	1.26±0.23	5.4	QSO B1426+015	Sy1	0.09	$2.41^{+0.74}_{-0.59}$	20.0	(3)
J1436.5+5847	219.149	58.798	1.37±0.16	8.3	QSO J1436+5847	Sy1	0.03	$1.68^{+0.27}_{-0.22}$	23.5	(2)
J1441.2+5330	220.300	53.500	0.85±0.16	5.1	Mrk 477	Sy2	0.04	$1.47^{+0.88}_{-0.46}$	24.0	(14)
J1442.6-1713	220.664	-17.223	4.83±0.34	14.4	**NGC 5728**	Sy2	0.01	$1.84^{+0.14}_{-0.14}$	24.3	(4)
J1453.1+2556	223.282	25.936	1.29±0.18	7.0	RX J1453.1+2554	Sy1	0.05	$1.82^{+0.26}_{-0.25}$	20.0	(2)
J1504.2+1025	226.073	10.417	1.51±0.22	6.8	Mrk 841	Sy1	0.04	$1.80^{+0.38}_{-0.36}$	21.3	(1)
J1515.4+4201	228.868	42.033	1.05±0.18	5.9	NGC 5899	Sy2	0.01	$1.72^{+0.56}_{-0.51}$	23.1	(2)
J1536.2+5753	234.061	57.890	1.43±0.18	7.9	Mrk 290	Sy1	0.03	$2.19^{+0.39}_{-0.34}$	20.4	(1)
J1548.4-1344	237.106	-13.749	2.91±0.39	7.4	NGC 5995	Sy2	0.03	$2.01^{+0.26}_{-0.24}$	22.0	(2)
J1554.8+3242	238.700	32.700	1.04±0.20	5.2	2MASX J15541741+3238381	Sy1	0.05	$1.66^{+0.76}_{-0.52}$	20.0	(2)
J1628.3+5147	247.082	51.793	2.45±0.20	12.4	SWIFT J1628.1+5145	Sy1.9	0.05	$2.13^{+0.19}_{-0.18}$	23.3	(1)
J1653.2+0224	253.319	2.404	4.20±0.35	12.1	**NGC 6240**	Sy2	0.02	$2.09^{+0.18}_{-0.17}$	24.3	(4)
J1822.1+6421	275.541	64.361	1.10±0.21	5.3	QSO B1821+643	Sy1	0.30	$2.91^{+0.97}_{-0.65}$	20.0	(15)
J1824.2-5620	276.057	-56.348	1.98±0.29	6.9	IC 4709	Sy2	0.02	$1.94^{+0.28}_{-0.26}$	23.1	(2)
J1835.1+3240	278.791	32.683	4.67±0.21	22.0	3C 382	Sy1	0.06	$2.09^{+0.11}_{-0.10}$	21.1	(1)
J1837.1-5922	279.284	-59.368	1.79±0.28	6.3	FAIRALL 49	Sy2	0.02	$2.55^{+0.43}_{-0.37}$	22.3	(14)
J1838.6-6523	279.658	-65.394	6.23±0.28	22.4	ESO 103-035	Sy2	0.01	$2.18^{+0.12}_{-0.12}$	23.2	(1)
J1842.4+7946	280.616	79.771	5.82±0.19	29.9	3C 390.3	Sy1	0.06	$1.95^{+0.07}_{-0.07}$	21.0	(1)
J1845.1-6223	281.297	-62.399	2.52±0.28	9.0	ESO 140-43	Sy1	0.01	$2.17^{+0.27}_{-0.25}$	22.4	(2)

Table 5—Continued

SWIFT NAME	R.A. (J2000)	DEC (J2000)	Flux [15-55 keV] (10^{-11} cgs)	S/N	ID	Type‡	redshift	Ph. Index (BAT only)	log(N_H)	Reference
J1857.3-7827	284.341	-78.464	1.86±0.26	7.1	LEDA 140831	Sy1	0.04	$1.85^{+0.36}_{-0.34}$	20.0	(2)
J1921.2-5840	290.323	-58.677	3.54±0.28	12.6	ESO 141-55	Sy1	0.04	$1.83^{+0.19}_{-0.18}$	20.0	(3)
J1942.7-1018	295.680	-10.316	4.30±0.30	14.3	NGC 6814	Sy1	0.01	$1.91^{+0.15}_{-0.14}$	20.8	(1)
J2009.1-6103	302.289	-61.064	3.03±0.26	11.5	SWIFT J2009.0-6103	Sy1	0.01	$1.98^{+0.21}_{-0.20}$	21.8	(1)
J2044.1-1043	311.039	-10.731	5.62±0.29	19.7	Mrk 509	Sy1.2	0.03	$2.04^{+0.12}_{-0.11}$	20.7	(1)
J2052.0-5703	313.017	-57.063	4.63±0.25	18.3	IC 5063	Sy2	0.01	$1.89^{+0.12}_{-0.12}$	23.3	(1)
J2109.1-0939	317.300	-9.652	1.58±0.27	5.9	1H 2107-097	Sy1	0.03	$2.15^{+0.40}_{-0.35}$	...	
J2132.1-3343	323.028	-33.727	2.92±0.27	10.7	CTS 109	Sy1	0.03	$2.07^{+0.22}_{-0.20}$	20.0	(2)
J2136.0-6223	324.006	-62.400	2.42±0.23	10.6	QSO J2136-6224	Sy1	0.06	$2.23^{+0.26}_{-0.24}$	20.0	(2)
J2138.8+3206	324.713	32.115	1.29±0.00	6.3	LEDA 67084	Sy1	0.03	$2.06^{+0.55}_{-0.48}$	20.0	(2)
J2200.7+1033	330.199	10.565	1.76±0.21	8.6	SWIFT J2200.9+1032	Sy1.9	0.03	$2.08^{+0.27}_{-0.25}$	22.2	(1)
J2202.1-3152	330.526	-31.878	8.01±0.25	31.8	NGC 7172	Sy2	0.01	$1.80^{+0.01}_{-0.01}$	22.9	(1)
J2204.5+0335	331.149	3.600	1.33±0.21	6.3	IRAS 22017+0319	Sy2	0.06	$2.29^{+0.48}_{-0.40}$	22.5	(2)
J2209.5-4709	332.387	-47.166	3.02±0.23	13.4	NGC 7213	Sy1.5	0.03	$1.92^{+0.17}_{-0.16}$	20.6	(1)
J2223.8-0207	335.962	-2.121	1.93±0.22	8.9	3C 445	Sy1	0.06	$1.99^{+0.24}_{-0.23}$	23.2	(2)
J2235.8-2603	338.966	-26.054	2.76±0.24	11.6	NGC 7314	Sy1.9	0.005	$2.04^{+0.20}_{-0.18}$	21.8	(1)
J2236.1+3357	339.040	33.952	1.66±0.19	8.8	Arp 319	Sy2	0.02	$1.75^{+0.27}_{-0.23}$	23.7	(2)
J2236.8-1235	339.223	-12.599	1.43±0.23	6.2	Mrk 915	Sy1	0.02	$1.59^{+0.33}_{-0.27}$	22.8	(2)
J2245.7+3941	341.449	39.695	1.71±0.18	9.2	3C 452	Sy2	0.08	$1.61^{+0.24}_{-0.19}$	23.4	(1)
J2254.1-1734	343.535	-17.578	5.67±0.23	24.7	MR 2251-178	Sy1	0.06	$2.06^{+0.13}_{-0.12}$	20.8	(1)
J2258.9+4053	344.749	40.899	1.31±0.18	7.2	UGC 12282	Sy1	0.02	$1.65^{+0.28}_{-0.22}$	23.9	(2)
J2259.5+2455	344.899	24.929	1.51±0.19	8.0	LEDA 70195	Sy1	0.03	$1.86^{+0.29}_{-0.28}$	20.0	(2)
J2303.2+0853	345.809	8.885	3.87±0.20	19.4	NGC 7469	Sy1.2	0.02	$2.14^{+0.12}_{-0.12}$	20.6	(1)
J2304.7-0841	346.194	-8.686	6.09±0.22	27.9	Mrk 926	Sy1.5	0.05	$1.97^{+0.01}_{-0.01}$	21.1	(1)
J2304.7+1217	346.200	12.300	1.11±0.20	5.6	NGC 7479	Sy2	0.01	$1.98^{+0.40}_{-0.37}$	23.6	(3)
J2318.4-4221	349.614	-42.360	4.09±0.20	20.7	**NGC 7582**	Sy2	0.01	$1.95^{+0.22}_{-0.24}$	24.1	(4)
J2319.0+0014	349.762	0.241	2.82±0.00	13.5	NGC 7603	Sy1	0.03	$2.07^{+0.18}_{-0.17}$	20.0	(2)
J2326.3+2154	351.600	21.900	0.97±0.19	5.1	RBS 2005	Sy1	0.12	$2.05^{+0.52}_{-0.47}$	20.3	(2)
J2342.0+3035	355.500	30.600	1.08±0.19	5.7	UGC 12741	Sy2	0.02	$1.64^{+0.33}_{-0.30}$	23.7	(2)

‡ The optical classification comes mainly from Tueller et al. (2008), Winter et al. (2009a), Parisi et al. (2009), Cusumano et al. (2010), SIMBAD, and NED.

References. — (1) Tueller et al. 2008; (2) This work: follow up with XRT; (3) This work: follow up with XMM; (4) See Tab. 3 for a detailed analysis of the Compton-thick sources. (5) Shinozaki et al. 2006; (6) Winter et al. 2009a; (7) Ueda et al. 2007; (8) Georgantopoulos et al. 2005; (9) Winter et al. 2009b; (10) Matt et al. 2009; (11) Cappi et al. 2006; (12) Page et al. 2005; (13) Winter et al. 2008; (14) Shu et al. 2007; (15) Jiménez-Bailón et al. 2007.